Asymptotic analysis of the potential energy difference because of a crack at a V-notch edge in a 3D domain

Brigit Mittelman and Zohar Yosibash

Pearlstone Center for Aeronautical Engineering Studies, Dept. of Mechanical Engineering Ben-Gurion University of the Negev, Beer-Sheva, 84105, Israel

Abstract

The difference in the potential energy in an elastic three-dimensional domain with a V-notch with and without a small crack ($\delta\Pi$) under a general mixed mode I+II+III loading is provided as an asymptotic series. It involves the V-notch edge stress intensity functions, the area of the formed crack, and special geometrical functions that can be pre-computed and tabulated. Importantly, the stress intensity functions along the crack front and the solution for the V-notched domain with the presence of the crack are un-necessary. The analytical formulation is verified by finite element methods, demonstrating the accuracy of the obtained expressions.

Keywords: Potential Energy, V-notch, edge stress intensity functions, 3D singularities

1. Introduction

Real life three dimensional (3D) structures often include cracks and V-notches that are subjected to mixed mode loading - in-plane tension (mode I), in-plane shear (mode II) and out-of-plane shear (mode III). These cannot be described adequately by 2D approximations (see for example the crack initiation at the edge of a V-notch in a PMMA specimen loaded in a four-point-loading configuration in Fig. 1). The classical theory of linear elastic fracture mechanics (LEFM) is aimed at predicting failure loads and direction in which a crack will propagate in brittle structures loaded quasi-statically. A variety of materials can be considered brittle, homogeneous and isotropic with good approximation. These include glasses, ceramics, and certain kinds of polymers (all of these usually encountered in engineering applications). For V-notches LEFM cannot be used directly, and generalization of LEFM concepts were published in recent years proposing several failure criteria for structures containing V-notch tips at which mechanical failures initiate (see e.g. [1, 2, 3, 4, 5]).

We present an asymptotic expansion for $\delta\Pi$ - the difference in the potential energy between a V-notched 3D linear elastic domain with and without a small crack (see Fig. 2). This expansion applies for all possible crack orientations initiating at any point along the V-notch edge (except for the vertices). Explicit elastic solutions for domains with a small crack inclined at any orientation at a V-notch tip is computationally intractable, so that an asymptotic expression for $\delta\Pi$ in 3D is mandatory for the determination of a failure criterion and failure initiation direction.

In a 2D domain, the asymptotic expression for $\delta\Pi$ under mixed modes I+II was presented in [6] as a constituent of a failure criterion at a V-notch. This failure criterion was demonstrated to well predict the failure initiation angle, and is chosen as the basis for further generalization to 3D loading conditions. This criterion is based on a small crack instantaneously created so it satisfies both strength requirement - the normal stress exceeds a critical value: $\sigma_n \geq \sigma_c$, and toughness requirement - a crack initiates along a direction at which $\delta\Pi$ is maximal and the incremental energy release rate reaches its critical value: $\mathcal{G} \geq \mathcal{G}_c$ [7]. It may be used also for formulating the toughness requirement in

Email address: zohary@bgu.ac.il (Brigit Mittelman and Zohar Yosibash)

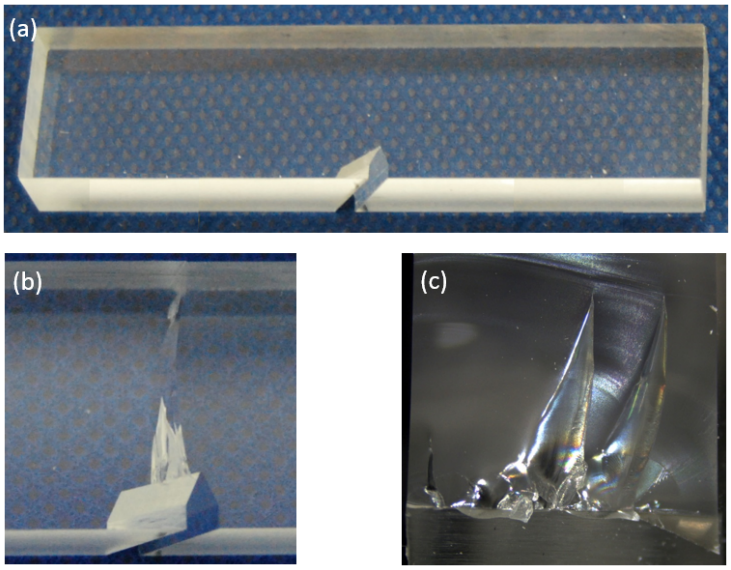

Figure 1: PMMA specimen before (a) and after fracture (b). (c) Zoom-in on the fracture surface.

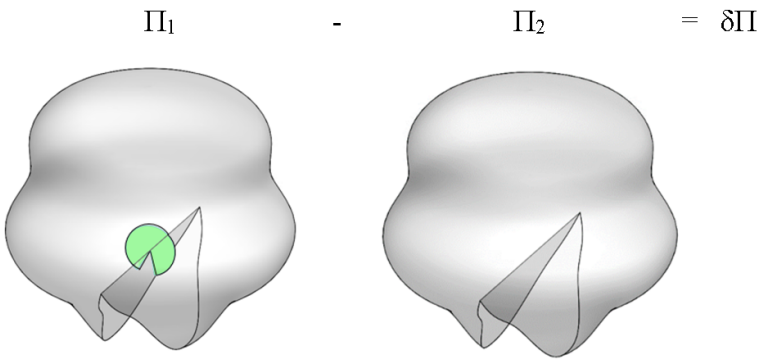

Figure 2: Considered domains for $\delta\Pi$.

3D: $-\frac{\delta\Pi}{S} \geq \mathcal{G}_c$, where S is the area of a crack surface, and $\mathcal{G}_c$ is the critical strain energy release rate which is a material property.

Preliminaries and notations are provided in Sec. 2, including the stress and displacement fields in the vicinity of a sharp V-notch within a 3D elastic isotropic domain. Sec. 3 details the asymptotic analysis which provides $\delta\Pi$ within a domain containing a V-notch, due to a small crack which initiates at a point along the notch edge. Detailed numerical methods for computation of all components required throughout the analysis are provided. Verification of the analysis is presented in Sec. 4 by comparing the asymptotic analysis to finite element (FE) results. Summary and conclusions are provided in Sec. 5.

2. Preliminaries and notations

Consider a linear elastic and isotropic 3D domain having a sharp V-notch with a straight edge. The 3D solution in the vicinity of the V-notch edge may be expressed by cylindrical coordinates (r, θ, z) , where the z axis coincides with the edge (Fig. 3). Spherical coordinates (ρ, φ, θ) with the origin at a chosen point $z = z_0$ can also be used

(Fig. 4). Throughout this work the notations were chosen so that the θ angle is the same in both cylindrical and spherical coordinate systems (and is offset by $-\pi/2$ with the conventional engineering terminology).

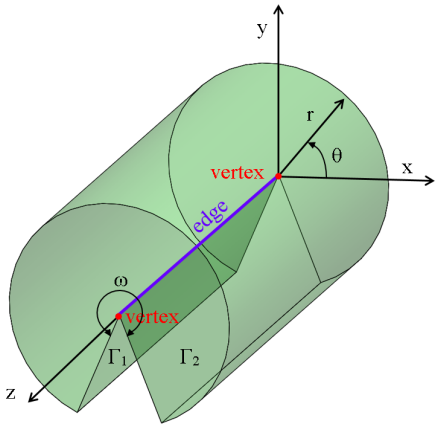

Figure 3: Edge and vertex singularities in a 3D domain.

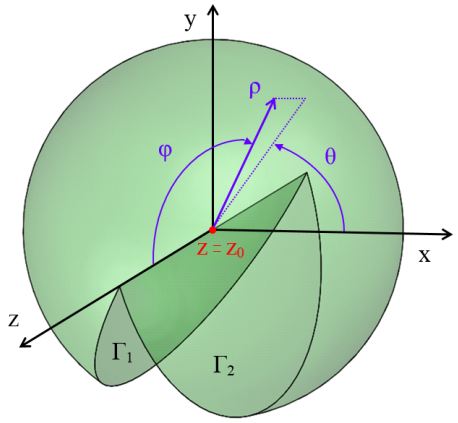

Figure 4: Spherical coordinates representation.

In the vicinity of a V-notch edge, the elastic solution (assuming no logarithmic terms ln(r)) is [8]:

$$\boldsymbol{u}(r,\theta,z) = \left\{ \begin{array}{c} u_r \\ u_\theta \\ u_z \end{array} \right\} = \sum_{i\geq 1}\sum_{j\geq 0} \partial_z^j A_i(z) r^{\alpha_i+j} \mathbf{s}_{ij}(\theta) \tag{1}$$

where α_i and $\mathbf{s}_{ij}(\theta)$ are called eigenpairs, $\mathbf{s}_{ij}(\theta) = \left\{ \begin{array}{c} s_r(\theta) \\ s_\theta(\theta) \\ s_z(\theta) \end{array} \right\}_{ij}$, and θ is measured so that $\frac{\pi}{2} + \frac{\omega}{2} \leq \theta \leq \frac{\pi}{2} - \frac{\omega}{2}$ ($\theta = 0$ on the the x axis see Fig. 3).

The corresponding stress vector is:

$$\boldsymbol{\sigma} = \left\{ \begin{array}{c} \sigma_{rr} \\ \sigma_{\theta\theta} \\ \sigma_{zz} \\ \sigma_{r\theta} \\ \sigma_{rz} \\ \sigma_{\theta z} \end{array} \right\} = \sum_{i\geq 1}\sum_{j\geq 0} \partial_z^j A_i(z) r^{\alpha_i+j-1} \mathbf{S}_{ij}(\theta) \tag{2}$$

The generalized edge stress intensity functions (GESIFs) $A_i(z)$ represent the strength of each singularity and may be computed by the quasi-dual function method [9].

For traction-free boundary conditions on both V-notch surfaces Γ_1, Γ_2 (see Fig. 3, 4) one has:

$$\left\{ \begin{array}{c} \mathcal{T}_r \\ \mathcal{T}_\theta \\ \mathcal{T}_z \end{array} \right\}_{\theta=\frac{\pi}{2}\pm\frac{\omega}{2}} = \left\{ \begin{array}{c} 0 \\ 0 \\ 0 \end{array} \right\} \quad \Rightarrow \quad \left\{ \begin{array}{c} \sigma_{r\theta} \\ \sigma_{\theta\theta} \\ \sigma_{\theta z} \end{array} \right\}_{\theta=\frac{\pi}{2}\pm\frac{\omega}{2}} = \left\{ \begin{array}{c} 0 \\ 0 \\ 0 \end{array} \right\} \tag{3}$$

For a V-notch solid angle ω and traction free boundary conditions on the V-notch surfaces, the first non zero eigenvalues α_1 and α_2 are determined by [8]:

$$sin^2(\alpha\omega) - \alpha^2 sin^2(\omega) = [sin(\alpha_1\omega) - \alpha_1 sin(\omega)] \times [sin(\alpha_2\omega) + \alpha_2 sin(\omega)] = 0 \tag{4}$$

and α_3 is determined by the non-trivial solution of the equation $\left(\alpha_3^2 + \frac{\partial^2}{\partial\theta^2}\right)(\mathbf{s}_z(\theta))_{30} = 0$. The eigen-values α_1 and α_2 are associated with the mode I and II of the 2D in-plane solutions (in a plane orthogonal to the V-notch singular edge) and α_3 corresponds to an out-of-plane solution ($\alpha_1 \leq \alpha_3 \leq \alpha_2$).

For traction-free V-notch surfaces and a V-notch angle of $\omega = 315^o$, for example, $\alpha_1 = 0.5050097$, $\alpha_2 = 0.6597016$, $\alpha_3 = 0.5714286$. The explicit solution for $\boldsymbol{u}$ in the vicinity of the edge is [8]:

$$\begin{aligned}
\boldsymbol{u}(r,\theta,z) \quad &= \quad \left\{ \begin{array}{c} u_r \\ u_\theta \\ u_z \end{array} \right\} = \boldsymbol{u^0}(0,\theta,z) \\
&+ \quad A_1(z)\, r^{\alpha_1} \left\{ \begin{array}{c} \left[cos[(1+\alpha_1)(\theta-\frac{\pi}{2})] + \frac{(\lambda+3\mu-\alpha_1(\lambda+\mu))}{(\lambda+\mu)(1-\alpha_1)} \frac{sin[\omega(1+\alpha_1)/2]}{sin[\omega(1-\alpha_1)/2]} cos[(1-\alpha_1)(\theta-\frac{\pi}{2})]\right] /2\mu\alpha_1 \left(\mathbf{S}_{\theta\theta}(\theta=\frac{\pi}{2})\right)_{10} \\ \left[-sin[(1+\alpha_1)(\theta-\frac{\pi}{2})] - \frac{(\lambda+3\mu+\alpha_1(\lambda+\mu))}{(\lambda+\mu)(1-\alpha_1)} \frac{sin[\omega(1+\alpha_1)/2]}{sin[\omega(1-\alpha_1)/2]} sin[(1-\alpha_1)(\theta-\frac{\pi}{2})]\right] /2\mu\alpha_1 \left(\mathbf{S}_{\theta\theta}(\theta=\frac{\pi}{2})\right)_{10} \\ 0 \end{array} \right\} \\
&+ \quad A_2(z)\, r^{\alpha_2} \left\{ \begin{array}{c} \left[sin[(1+\alpha_2)(\theta-\frac{\pi}{2})] + \frac{(\lambda+3\mu-\alpha_2(\lambda+\mu))}{(\lambda+\mu)(1+\alpha_2)} \frac{sin[\omega(1+\alpha_2)/2]}{sin[\omega(1-\alpha_2)/2]} sin[(1-\alpha_2)(\theta-\frac{\pi}{2})]\right] /2\mu\alpha_2 \left(\mathbf{S}_{r\theta}(\theta=\frac{\pi}{2})\right)_{20} \\ \left[cos[(1+\alpha_2)(\theta-\frac{\pi}{2})] + \frac{(\lambda+3\mu+\alpha_2(\lambda+\mu))}{(\lambda+\mu)(1+\alpha_2)} \frac{sin[\omega(1+\alpha_2)/2]}{sin[\omega(1-\alpha_2)/2]} cos[(1-\alpha_2)(\theta-\frac{\pi}{2})]\right] /2\mu\alpha_2 \left(\mathbf{S}_{r\theta}(\theta=\frac{\pi}{2})\right)_{20} \\ 0 \end{array} \right\} \\
&+ \quad A_3(z)\, r^{\alpha_3} \frac{\omega}{\pi\mu} \left\{ \begin{array}{c} 0 \\ 0 \\ sin[\frac{\pi}{\omega}(\theta-\frac{\pi}{2})] \end{array} \right\} + O\left(r^1\right)
\end{aligned} \tag{5}$$

where λ, μ are the Lamé constants, $\boldsymbol{u}^0(0,\theta,z)$ represents the rigid body motions, and we used the notations $\left(\mathbf{S}_{\theta\theta}(\theta=\frac{\pi}{2})\right)_{10} = \frac{(1+\alpha_1)}{(1-\alpha_1)} \frac{sin[\omega(1+\alpha_1)/2]}{sin[\omega(1-\alpha_1)/2]} - 1$, $\left(\mathbf{S}_{r\theta}(\theta=\frac{\pi}{2})\right)_{20} = 1 - \frac{(1-\alpha_2)}{(1+\alpha_2)} \frac{sin[\omega(1+\alpha_2)/2]}{sin[\omega(1-\alpha_2)/2]}$ which are normalization factors for the stresses so that for mode I $\left(\mathbf{S}_{\theta\theta}(\theta=\frac{\pi}{2})\right)_{10} = 1$ and for mode II $\left(\mathbf{S}_{r\theta}(\theta=\frac{\pi}{2})\right)_{20} = 1$.

The explicit stress field corresponding to (5) is:

$$
\begin{aligned}
\boldsymbol{\sigma}(r,\theta,z) &= \left\{ \begin{array}{c} \sigma_{rr} \\ \sigma_{\theta\theta} \\ \sigma_{zz} \\ \sigma_{r\theta} \\ \sigma_{rz} \\ \sigma_{\theta z} \end{array} \right\} \\
&= A_1(z)\, r^{\alpha_1-1} \left\{ \begin{array}{c} \Big[cos[(1+\alpha_1)(\theta-\frac{\pi}{2})] + \frac{(3-\alpha_1)}{(1-\alpha_1)} \frac{sin[\omega(1+\alpha_1)/2]}{sin[\omega(1-\alpha_1)/2]} cos[(1-\alpha_1)(\theta-\frac{\pi}{2})]\Big] / \left(\mathbf{S}_{\theta\theta}(\theta=\frac{\pi}{2})\right)_{10} \\ \Big[-cos[(1+\alpha_1)(\theta-\frac{\pi}{2})] + \frac{(1+\alpha_1)}{(1-\alpha_1)} \frac{sin[\omega(1+\alpha_1)/2]}{sin[\omega(1-\alpha_1)/2]} cos[(1-\alpha_1)(\theta-\frac{\pi}{2})^*]\Big] / \left(\mathbf{S}_{\theta\theta}(\theta=\frac{\pi}{2})\right)_{10} \\ \frac{2\lambda}{\lambda+\mu} \frac{sin[\omega(1+\alpha_1)/2]}{sin[\omega(1-\alpha_1)/2]} \frac{cos[(1-\alpha_1)(\theta-\frac{\pi}{2})]}{1-\alpha_1} / \left(\mathbf{S}_{\theta\theta}(\theta=\frac{\pi}{2})\right)_{10} \\ \Big[-sin[(1+\alpha_1)(\theta-\frac{\pi}{2})] + \frac{sin[\omega(1+\alpha_1)/2]}{sin[\omega(1-\alpha_1)/2]} sin[(1-\alpha_1)(\theta-\frac{\pi}{2})]\Big] / \left(\mathbf{S}_{\theta\theta}(\theta=\frac{\pi}{2})\right)_{10} \\ 0 \\ 0 \end{array} \right\} \\
&+ A_2(z)\, r^{\alpha_2-1} \left\{ \begin{array}{c} \Big[sin[(1+\alpha_2)(\theta-\frac{\pi}{2})] + \frac{(3-\alpha_2)}{(1+\alpha_2)} \cdot \frac{sin[\omega(1+\alpha_2)/2]}{sin[\omega(1-\alpha_2)/2]} sin[(1-\alpha_2)(\theta-\frac{\pi}{2})]\Big] / \left(\mathbf{S}_{r\theta}(\theta=\frac{\pi}{2})\right)_{20} \\ \Big[-sin[(1+\alpha_2)(\theta-\frac{\pi}{2})] + \frac{sin[\omega(1+\alpha_2)/2]}{sin[\omega(1-\alpha_2)/2]} sin[(1-\alpha_2)(\theta-\frac{\pi}{2})]\Big] / \left(\mathbf{S}_{r\theta}(\theta=\frac{\pi}{2})\right)_{20} \\ \frac{2\lambda}{\lambda+\mu} \frac{sin[\omega(1+\alpha_2)/2]}{sin[\omega(1-\alpha_2)/2]} \frac{sin[(1-\alpha_2)(\theta-\frac{\pi}{2})]}{1+\alpha_2} / \left(\mathbf{S}_{r\theta}(\theta=\frac{\pi}{2})\right)_{20} \\ \Big[cos[(1+\alpha_2)(\theta-\frac{\pi}{2})] - \frac{(1-\alpha_2)}{(1+\alpha_2)} \frac{sin[\omega(1+\alpha_2)/2]}{sin[\omega(1-\alpha_2)/2]} cos[(1-\alpha_2)(\theta-\frac{\pi}{2})]\Big] / \left(\mathbf{S}_{r\theta}(\theta=\frac{\pi}{2})\right)_{20} \\ 0 \\ 0 \end{array} \right\} \\
&+ A_3(z)\, r^{\alpha_3-1} \left\{ \begin{array}{c} 0 \\ 0 \\ 0 \\ 0 \\ sin[\frac{\pi}{\omega}(\theta-\frac{\pi}{2})] \\ cos[\frac{\pi}{\omega}(\theta-\frac{\pi}{2})] \end{array} \right\} \\
&+ O(r^0)
\end{aligned}
\tag{6}
$$

3. Asymptotic representation of $\delta\Pi$ because of a crack initiating at the V-notch edge

Let us consider $\delta\Pi$, the difference in the potential energy between a V-notched domain with and without a small crack created at its tip (see Fig. 5). Since it is practically impossible to compute the explicit elastic solution for the domain with a small crack inclined at all different angles at a V-notch tip, there is a need for an asymptotic expansion to provide an asymptotic approximation for $\delta\Pi$ [7, 6].

3.1. Asymptotic representation of displacements in the "far" and "near" domains

A "far" (outer) elastic solution denotes the solution as if a small crack does not exist and we have a V-notch without the crack at $r \to 0$. This solution clearly serves as a better approximation as one moves away from the small crack, or - outside the cracks' surroundings, and therefore is named the far (outer) solution. To resolve the dependence on the small crack area S , the domain coordinates are "stretched" by $\frac{1}{\sqrt{S}}$:

$$\rho^* = \frac{\rho}{\sqrt{S}} \tag{7}$$

As $\sqrt{S} \to 0$, an unbounded domain $\rho^* = \frac{\rho}{\sqrt{S}}$ is obtained, in which the crack area equals 1. The solution can now be otherwise represented, in the form of a "near" (inner) field, which represents an elastic solution for a V-notched domain with a small crack initiating at a point along its edge. This solution serves as a better approximation as one moves towards the crack, and therefore is named the near (inner) solution.

We consider a point z_0 along the V-notch front where a small crack may initiate, and locate there the spherical coordinate system (ρ, φ, θ) (see Fig. 3, 4). At $z = z_0$ the far field displacements (as if no crack exists) is:

$$\begin{aligned} \boldsymbol{u}^{far}(r,\theta,z) &= \boldsymbol{u}^0(0,0,0) + A_1(z_0) \times r^{\alpha_1} \times \boldsymbol{s}_{10}(\theta) + A_2(z_0) \times r^{\alpha_2} \times \boldsymbol{s}_{20}(\theta) + A_3(z_0) \times r^{\alpha_3} \times \boldsymbol{s}_{30}(\theta) + ... \\ &= \boldsymbol{u}^0(0,0,0) + A_1(z_0) \times (\rho\, sin\varphi)^{\alpha_1} \times \boldsymbol{s}_{10}(\theta) + A_2(z_0) \times (\rho\, sin\varphi)^{\alpha_2} \times \boldsymbol{s}_{20}(\theta) \\ &\quad + A_3(z_0) \times (\rho\, sin\varphi)^{\alpha_3} \times \boldsymbol{s}_{30}(\theta) + ... \\ &= \boldsymbol{u}^{far}(\rho,\varphi,\theta) \end{aligned} \tag{8}$$

where $\boldsymbol{u}^0(0,0,0)$ represents the rigid body motion, and the terms $\boldsymbol{s}_{20}, \boldsymbol{s}_{20}$ and $\boldsymbol{s}_{30}$ are explicitly presented in (5). The stretched spherical domain around the point (z_0) is considered next (an "inflated point"), where $r^* = \rho^* sin(\varphi)$. By substituting (7) in (8) one obtains:

$$\begin{aligned} \boldsymbol{u}^{far}(\rho^*\sqrt{S},\varphi,\theta) &= \boldsymbol{u}^0(0,0,0) + A_1 \times (\sqrt{S})^{\alpha_1} \times (\rho^* sin\varphi)^{\alpha_1} \times \boldsymbol{s}_{10}(\theta) + A_2 \times (\sqrt{S})^{\alpha_2} \times (\rho^* sin\varphi)^{\alpha_2} \times \boldsymbol{s}_{20}(\theta) \\ &\quad + A_3 \times (\sqrt{S})^{\alpha_3} \times (\rho^* sin\varphi)^{\alpha_3} \times \boldsymbol{s}_{30}(\theta) + ... \end{aligned} \tag{9}$$

The 3D near field domain is a sphere around the notch tip denoted Ω_c^* in which a planar crack exists (Fig. 5), and by constructions $S^* = 1$ (S^* is the crack area in Ω_c^*).

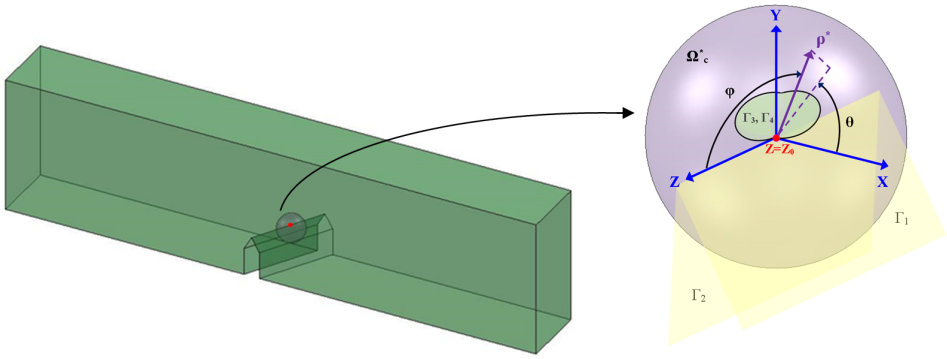

Figure 5: The outer and inner expansions in 3D

The far and near field expansions must be matched appropriately at $\rho^* \to \infty$. The near field asymptotic expansion in Ω_c^* , similarly to the 2D asymptotic expansion derived in [6], is assumed to be represented by:

$$\begin{aligned} \boldsymbol{u}^{near}(\rho,\varphi,\theta) &= \boldsymbol{u}^{near}(\rho^*\sqrt{S},\varphi,\theta) \\ &= d_0(\sqrt{S}) \times \mathbf{V}_0(\rho^*,\varphi,\theta) + d_1(\sqrt{S}) \times \mathbf{V}_1(\rho^*,\varphi,\theta) + d_2(\sqrt{S}) \times \mathbf{V}_2(\rho^*,\varphi,\theta) + d_3(\sqrt{S}) \times \mathbf{V}_3(\rho^*,\varphi,\theta) + ... \end{aligned} \tag{10}$$

Matching of the far and near fields as $\rho^* \to \infty$ imposes the following terms in the asymptotic series (10):

$$\begin{aligned} d_0(\sqrt{S}) &= 1, \quad \mathbf{V}_0(\rho^*,\varphi,\theta) = \boldsymbol{u}^0(0,0,0) \\ d_1(\sqrt{S}) &= A_1 \times (\sqrt{S})^{\alpha_1}, \quad \mathbf{V}_1(\rho^*,\varphi,\theta) \sim (\rho^* sin\varphi)^{\alpha_1} \times \boldsymbol{s}_{10}(\theta) \\ d_2(\sqrt{S}) &= A_2 \times (\sqrt{S})^{\alpha_2}, \quad \mathbf{V}_2(\rho^*,\varphi,\theta) \sim (\rho^* sin\varphi)^{\alpha_2} \times \boldsymbol{s}_{20}(\theta) \\ d_3(\sqrt{S}) &= A_3 \times (\sqrt{S})^{\alpha_3}, \quad \mathbf{V}_3(\rho^*,\varphi,\theta) \sim (\rho^* sin\varphi)^{\alpha_3} \times \boldsymbol{s}_{30}(\theta) \end{aligned} \tag{11}$$

It terms of "regular" coordinates (ρ, φ, θ) or (r, θ, z) , the domain Ω_c^* is small and represents an "inflated point", and since the GESIFs $A_i(z)$ are smooth functions along the edge, $A_i(z) = A_i(z_0) \equiv A_i = const$.

It terms of "normalized" coordinates $(\rho^*, \varphi, \theta)$, Ω_c^* is infinitely large. To match the inner solution as $\rho^* \to \infty$, the terms $\mathbf{V}_i(\rho^*, \varphi, \theta)$ are expressed by:

$$\mathbf{V}_i(\rho^*,\varphi,\theta) = (\rho^* sin\rho)^{\alpha_i} \times \boldsymbol{s}_{i\,0}(\theta) + \hat{\mathbf{V}}_i(\rho^*,\varphi,\theta) \quad i = 1,2,3 \tag{12}$$

in which $\hat{\mathbf{V}}_i$ is bounded, i.e. $\hat{\mathbf{V}}_i(\rho^*,\varphi,\theta) \overset{\rho^*\to\infty}{\longrightarrow} 0$. The solution $\mathbf{V}_i$ in (12) can be therefore composed of the solution in the vicinity of a V-notch tip + a term $\hat{\mathbf{V}}_i$ confined to the Ω_c^* domain, which is added by the presence of the crack. Substituting (11)-(12) in (10) one obtains:

$$\begin{aligned}\boldsymbol{u}^{near}(\rho^*\sqrt{S},\varphi,\theta) \;=\; & \boldsymbol{u}^0(0,0,0) + A_1\times(\sqrt{S})^{\alpha_1}\times[(\rho^* sin\varphi)^{\alpha_1}\times \boldsymbol{s}_{10}(\theta) + \hat{\mathbf{V}}_1(\rho^*,\varphi,\theta)] \\ & + A_2\times(\sqrt{S})^{\alpha_2}\times[(\rho^* sin\varphi)^{\alpha_2}\times \boldsymbol{s}_{20}(\theta) + \hat{\mathbf{V}}_2(\rho^*,\varphi,\theta)] \\ & + A_3\times(\sqrt{S})^{\alpha_3}\times[(\rho^* sin\varphi)^{\alpha_3}\times \boldsymbol{s}_{30}(\theta) + \hat{\mathbf{V}}_3(\rho^*,\varphi,\theta)] + ... \end{aligned} \tag{13}$$

As $\rho^*\to\infty$ $\mathbf{V}_i$ in the near field coincides with the far field as $\rho\to 0$ (the near field and far field solutions are matched). $\mathbf{V}_i$ satisfies the elasticity problem and therefore, $\hat{\mathbf{V}}_i$ has to satisfy (see Figure 5):

$$\mathcal{L}(\mathbf{V}_i) = \mathcal{L}((\rho^* sin\varphi)^{\alpha_i}\times \boldsymbol{s}_{i0}(\theta)) + \mathcal{L}(\hat{\mathbf{V}}_i) = 0 \;\Rightarrow \mathcal{L}(\hat{\mathbf{V}}_i) = 0 \;\text{ in}\,\Omega_c^* \tag{14}$$

$$\mathcal{T}(\mathbf{V}_i) = \mathcal{T}((\rho^* sin\varphi)^{\alpha_i}\times \boldsymbol{s}_{i0}(\theta)) + \mathcal{T}(\hat{\mathbf{V}}_i) = 0 \;\Rightarrow \mathcal{T}(\hat{\mathbf{V}}_i) = 0 \;\text{ on}\,\Gamma_1,\Gamma_2 \tag{15}$$

$$\mathcal{T}(\mathbf{V}_i) = \mathcal{T}((\rho^* sin\varphi)^{\alpha_i}\times \boldsymbol{s}_{i0}(\theta)) + \mathcal{T}(\hat{\mathbf{V}}_i) = 0 \;\Rightarrow \mathcal{T}(\hat{\mathbf{V}}_i) = -\mathcal{T}((\rho^* sin\varphi)^{\alpha_i}\times \boldsymbol{s}_{i0}(\theta)) \;\text{ on}\,\Gamma_3,\Gamma_4 \tag{16}$$

$$\sigma(\hat{\mathbf{V}}_i) \underset{\rho^*\to\infty}{\sim} 0 \text{ or } \hat{\mathbf{V}}_i \underset{\rho^*\to\infty}{\sim} 0 \tag{17}$$

where Γ_1,Γ_2 are the V-notch faces, Γ_3,Γ_4 are the crack faces, $\mathcal{T}_i = \sigma_{ij}\hat{n}_j$ and $\mathcal{L}$ represents the Navier-Lamé operator (see [8] eq. (13.5), (13.22)). $\hat{\boldsymbol{n}} = (n_x, n_y, n_z)$ is the unit normal vector which describes the unit area crack orientation.

The change in potential energy due to the creation of a crack of area S in the V-notched domain at $z = z_0$ is expressed by (see derivation in Appendix A):

$$\delta\Pi = \Psi\left[\boldsymbol{u}^{near}, \boldsymbol{u}^{far}\right] \overset{\triangle}{=} -\tfrac{1}{2}\int_{\Gamma^{sph}} \left(\mathcal{T}(\boldsymbol{u}^{near})\boldsymbol{u}^{far} - \mathcal{T}(\boldsymbol{u}^{far})\boldsymbol{u}^{near}\right) d\Gamma \tag{18}$$

where Γ^{sph} is the spherical part of the inner domain (the crack and V-notch surfaces do not contribute to the surface integral). Inserting (9) and (13) in (18) and using the linearity property of the functional Ψ one obtains:

$$\begin{aligned}\delta\Pi \;=\; & \Psi[\boldsymbol{u}^0(0,0,0), \boldsymbol{u}^0(0,0,0)] + \Psi[\boldsymbol{u}^0(0,0,0)\,,\, A_1\times(\sqrt{S})^{\alpha_1}\times(\rho^* sin\varphi)^{\alpha_1}\times \boldsymbol{s}_{10}(\theta)] \\ & + \Psi[\boldsymbol{u}^0(0,0,0), A_2\times(\sqrt{S})^{\alpha_2}\times(\rho^* sin\varphi)^{\alpha_2}\times \boldsymbol{s}_{20}(\theta)] + \Psi[\boldsymbol{u}^0(0,0,0), A_3\times(\sqrt{S})^{\alpha_3}\times(\rho^* sin\varphi)^{\alpha_3}\times \boldsymbol{s}_{30}(\theta)] \\ & + \Psi[A_1\times(\sqrt{S})^{\alpha_1}\times\left((\rho^* sin\varphi)^{\alpha_1}\times \boldsymbol{s}_{10}(\theta) + \hat{\mathbf{V}}_1(\rho^*,\varphi,\theta)\right), \boldsymbol{u}^0(0,0,0)] \\ & + \Psi[A_1\times(\sqrt{S})^{\alpha_1}\times\left((\rho^* sin\varphi)^{\alpha_1}\times \boldsymbol{s}_{10}(\theta) + \hat{\mathbf{V}}_1(\rho^*,\varphi,\theta)\right), A_1\times(\sqrt{S})^{\alpha_1}\times(\rho^* sin\varphi)^{\alpha_1}\times \boldsymbol{s}_{1\,0}(\theta)] \\ & + \Psi[A_1\times(\sqrt{S})^{\alpha_1}\times\left((\rho^* sin\varphi)^{\alpha_1}\times \boldsymbol{s}_{10}(\theta) + \hat{\mathbf{V}}_1(\rho^*,\varphi,\theta)\right), A_2\times(\sqrt{S})^{\alpha_2}\times(\rho^* sin\varphi)^{\alpha_2}\times \boldsymbol{s}_{20}(\theta)] \\ & + \Psi[A_1\times(\sqrt{S})^{\alpha_1}\times\left((\rho^* sin\varphi)^{\alpha_1}\times \boldsymbol{s}_{10}(\theta) + \hat{\mathbf{V}}_1(\rho^*,\varphi,\theta)\right), A_3\times(\sqrt{S})^{\alpha_3}\times(\rho^* sin\varphi)^{\alpha_3}\times \boldsymbol{s}_{30}(\theta)] \\ & + \Psi[A_2\times(\sqrt{S})^{\alpha_2}\times\left((\rho^* sin\varphi)^{\alpha_2}\times \boldsymbol{s}_{20}(\theta) + \hat{\mathbf{V}}_2(\rho^*,\varphi,\theta)\right), \boldsymbol{u}^0(0,0,0)] \\ & + \Psi[A_2\times(\sqrt{S})^{\alpha_2}\times\left((\rho^* sin\varphi)^{\alpha_2}\times \boldsymbol{s}_{20}(\theta) + \hat{\mathbf{V}}_2(\rho^*,\varphi,\theta)\right), A_1\times(\sqrt{S})^{\alpha_1}\times(\rho^* sin\varphi)^{\alpha_1}\times \boldsymbol{s}_{10}(\theta)] \\ & + \Psi[A_2\times(\sqrt{S})^{\alpha_2}\times\left((\rho^* sin\varphi)^{\alpha_2}\times \boldsymbol{s}_{20}(\theta) + \hat{\mathbf{V}}_2(\rho^*,\varphi,\theta)\right), A_2\times(\sqrt{S})^{\alpha_2}\times(\rho^* sin\varphi)^{\alpha_2}\times \boldsymbol{s}_{20}(\theta)] \\ & + \Psi[A_2\times(\sqrt{S})^{\alpha_2}\times\left((\rho^* sin\varphi)^{\alpha_2}\times \boldsymbol{s}_{20}(\theta) + \hat{\mathbf{V}}_2(\rho^*,\varphi,\theta)\right), A_3\times(\sqrt{S})^{\alpha_3}\times(\rho^* sin\varphi)^{\alpha_3}\times \boldsymbol{s}_{30}(\theta)] \\ & + \Psi[A_3\times(\sqrt{S})^{\alpha_3}\times\left((\rho^* sin\varphi)^{\alpha_3}\times \boldsymbol{s}_{30}(\theta) + \hat{\mathbf{V}}_3(\rho^*,\varphi,\theta)\right), \boldsymbol{u}^0(0,0,0)] \\ & + \Psi[A_3\times(\sqrt{S})^{\alpha_3}\times(\rho^* sin\varphi)^{\alpha_3}\times \boldsymbol{s}_{30}(\theta) + \hat{\mathbf{V}}_3(\rho^*,\varphi,\theta)\,,\, A_1\times(\sqrt{S})^{\alpha_1}\times(\rho^* sin\varphi)^{\alpha_1}\times \boldsymbol{s}_{10}(\theta)] \\ & + \Psi[A_3\times(\sqrt{S})^{\alpha_3}\times(\rho^* sin\varphi)^{\alpha_3}\times \boldsymbol{s}_{30}(\theta) + \hat{\mathbf{V}}_3(\rho^*,\varphi,\theta)\,,\, A_2\times(\sqrt{S})^{\alpha_2}\times(\rho^* sin\varphi)^{\alpha_2}\times \boldsymbol{s}_{20}(\theta)] \\ & + \Psi[A_3\times(\sqrt{S})^{\alpha_3}\times(\rho^* sin\varphi)^{\alpha_3}\times \boldsymbol{s}_{30}(\theta) + \hat{\mathbf{V}}_3(\rho^*,\varphi,\theta)\,,\, A_3\times(\sqrt{S})^{\alpha_3}\times(\rho^* sin\varphi)^{\alpha_3}\times \boldsymbol{s}_{30}(\theta)] \\ & + \text{high order terms (H.O.T)} \end{aligned} \tag{19}$$

After some technical manipulations (see Appendix B), expression (20) is reduced to:

$$
\begin{aligned}
\delta\Pi \;=\;& A_1^2 \times (\sqrt{S})^{2\alpha_1} \times \Psi[\hat{\mathbf{V}}_1(\rho^*,\varphi,\theta)\,,\,(\rho^* sin\varphi)^{\alpha_1} \times \boldsymbol{s}_{10}(\theta)] \\
&+A_1 \times A_2 \times (\sqrt{S})^{\alpha_1+\alpha_2} \times \Psi[\hat{\mathbf{V}}_1(\rho^*,\varphi,\theta)\,,\,(\rho^* sin\varphi)^{\alpha_2} \times \boldsymbol{s}_{20}(\theta)] \\
&+A_1 \times A_3 \times (\sqrt{S})^{\alpha_1+\alpha_3} \times \Psi[\hat{\mathbf{V}}_1(\rho^*,\varphi,\theta)\,,\,(\rho^* sin\varphi)^{\alpha_3} \times \boldsymbol{s}_{30}(\theta)] \\
&+A_1 \times A_2 \times (\sqrt{S})^{\alpha_1+\alpha_2} \times \Psi[\hat{\mathbf{V}}_2(\rho^*,\varphi,\theta)\,,\,(\rho^* sin\varphi)^{\alpha_1} \times \boldsymbol{s}_{10}(\theta)] \\
&+A_2^2 \times (\sqrt{S})^{2\alpha_2} \times \Psi[\hat{\mathbf{V}}_2(\rho^*,\varphi,\theta)\,,\,(\rho^* sin\varphi)^{\alpha_2} \times \boldsymbol{s}_{20}(\theta)] \\
&+A_2 \times A_3 \times (\sqrt{S}))^{\alpha_2+\alpha_3} \times \Psi[\hat{\mathbf{V}}_2(\rho^*,\varphi,\theta)\,,\,(\rho^* sin\varphi)^{\alpha_3} \times \boldsymbol{s}_{30}(\theta)] \\
&+A_1 \times A_3 \times (\sqrt{S})^{\alpha_1+\alpha_3} \times \Psi[\hat{\mathbf{V}}_3(\rho^*,\varphi,\theta)\,,\,(\rho^* sin\varphi)^{\alpha_1} \times \boldsymbol{s}_{10}(\theta)] \\
&+A_2 \times A_3 \times (\sqrt{S}))^{\alpha_2+\alpha_3} \times \Psi[\hat{\mathbf{V}}_3(\rho^*,\varphi,\theta)\,,\,(\rho^* sin\varphi)^{\alpha_2} \times \boldsymbol{s}_{20}(\theta)] \\
&+A_3^2 \times (\sqrt{S})^{2\alpha_3} \times \Psi[\hat{\mathbf{V}}_3(\rho^*,\varphi,\theta)\,,\,(\rho^* sin\varphi)^{\alpha_3} \times \boldsymbol{s}_{30}(\theta)] + H.O.T.
\end{aligned} \tag{20}
$$

or in general:

$$
\delta\Pi = \sum_i \sum_j A_i\, A_j \times (\sqrt{S})^{\alpha_i+\alpha_j}\, \Psi[\hat{\mathbf{V}}_i\,,\,(\rho^* sin\varphi)^{\alpha_j}\, \boldsymbol{s}_{j0}(\theta)] + H.O.T. \quad \text{for}\, i,j = 1,2,3 \tag{21}
$$

The expression for $\delta\Pi$ involves $\hat{\mathbf{V}}_i$ defined in the near domain. Therefore we consider the integrals $\Psi[\hat{\mathbf{V}}_i\,,\,(\rho^* sin\varphi)^{\alpha_j} \times \boldsymbol{s}_{j0}(\theta)]$ over the sphere Γ^*_{sph} for $\rho^* = R \to \infty$. By definition (18):

$$
\Psi[\hat{\mathbf{V}}_i, (\rho^* sin\varphi)^{\alpha_j} \times \boldsymbol{s}_{j0}(\theta)] \triangleq -\frac{1}{2} \int\limits_{\Gamma^{sph}} \left(\mathcal{T}(\hat{\mathbf{V}}_i) \times (\rho^* sin\varphi)^{\alpha_j} \times \boldsymbol{s}_{j0}(\theta) - \mathcal{T}\left((\rho^* sin\varphi)^{\alpha_j} \times \boldsymbol{s}_{j0}(\theta)\right) \times \hat{\mathbf{V}}_i \right) d\Gamma \tag{22}
$$

Because $\hat{\mathbf{V}}_i = 0$ on the sphere at which $\rho^* \to \infty$, (22) reduces to:

$$
\Psi[\hat{\mathbf{V}}_i\,,\,(\rho^* sin\varphi)^{\alpha_j} \times \boldsymbol{s}_{j0}(\theta)] = -\frac{1}{2} \int\limits_{\Gamma^{sph}} \mathcal{T}(\hat{\mathbf{V}}_i) \times (\rho^* sin\varphi)^{\alpha_j} \times \boldsymbol{s}_{j0}(\theta)\, d\Gamma \tag{23}
$$

Note that:

$$
d\Gamma = \rho^2 sin\varphi\, d\varphi\, d\theta = (\rho^* \sqrt{S})^2 sin\varphi\, d\varphi\, d\theta = S\,(\rho^*)^2 sin\varphi\, d\varphi\, d\theta = S\, d\Gamma^* \tag{24}
$$

Observe that the angles θ, φ do not change in the coordinate transformation in the "stretched" domain.

The coordinate transformation also necessitates to consider the $\mathcal{T}(\bullet)$ operator. By the chain rule: $\frac{d(\bullet)}{d\rho} = \frac{d(\bullet)}{d\rho^*}\frac{d\rho^*}{d\rho} = \frac{d(\bullet)}{d\rho^*}\frac{1}{\sqrt{S}}$. For the other derivatives $\frac{d(\bullet)}{\rho d\varphi} = \frac{d(\bullet)}{(\rho^*\sqrt{S})\, d\varphi} = \frac{d(\bullet)}{\rho^* d\varphi}\frac{1}{\sqrt{S}}$ and similarly $\frac{d(\bullet)}{\rho\, sin(\varphi)\, d\theta} = \frac{d(\bullet)}{(\rho^*\sqrt{S}) \times sin(\varphi)\, d\theta} = \frac{d(\bullet)}{\rho^* sin(\varphi)\, d\theta}\frac{1}{\sqrt{S}}$. We can therefore conclude that $\mathcal{T}(\hat{\mathbf{V}}_i) = \frac{1}{\sqrt{S}}\mathcal{T}^*(\hat{\mathbf{V}}_i)$ (where $\mathcal{T}$ and $\mathcal{T}^*$ represent the traction operators in the un-stretched and stretched coordinates, respectively).

With these definitions (23) becomes:

$$
\Psi[\hat{\mathbf{V}}_i\,,\,(\rho^* sin\varphi)^{\alpha_j} \times \boldsymbol{s}_{j0}(\theta)] = \left[-\tfrac{1}{2} \int\limits_{\Gamma^{*sph}} \left(\mathcal{T}^*(\hat{\mathbf{V}}_i) \times (\rho^* sin\varphi)^{\alpha_j} \times \boldsymbol{s}_{j0}(\theta) \right) \times (\rho^*)^2 sin\varphi\, d\varphi\, d\theta \right] \sqrt{S} \tag{25}
$$

We define:

$$
\begin{aligned}
H_{ij} \;&\triangleq\; -\Psi\left[\hat{\mathbf{V}}_i(\rho^*,\varphi,\theta), (\rho^* sin\varphi)^{\alpha_j} \times \boldsymbol{s}_{j0}(\theta)\right] / \sqrt{S} \\
&=\; \frac{1}{2} \int\limits_{\Gamma^{*sph}} \left(\mathcal{T}^*(\hat{\mathbf{V}}_i) \times (\rho^* sin\varphi)^{\alpha_j} \times \boldsymbol{s}_{j0}(\theta) \right) \times (\rho^*)^2 sin\varphi\, d\varphi\, d\theta
\end{aligned} \tag{26}
$$

One notices that H_{ij} depend on ω, θ, φ and material properties, and may be computed by a FE model of a sphere with outer radius $\rho^* \to \infty$, containing a V-notch and a crack located at its center and inclined at the angles φ, θ.

Remark 1. *One may seek either* $\mathbf{V}_i$ *or* $\hat{\mathbf{V}}_i$ *. For the calculation of the* H_{ij} *, the* $\hat{\mathbf{V}}_i$ *solution was considered in* Ω_c^* *. This dictated traction boundary conditions on the crack faces (16), and clamped boundary conditions over the outer surface of* Ω_c^* *(17). If* $\mathbf{V}_i$ *would had been sought, the crack faces within* Ω_c^* *would have been traction free and on the outer surface of the domain, the solution would had approach that of a V-notch with no crack* $(\mathbf{V}_i \overset{\rho^*\to\infty}{\longrightarrow} (\rho^* sin\rho)^{\alpha_i} \times \boldsymbol{s}_{i\,0}(\theta))$

Inserting (25) and (26) in (20) one obtains:

$$\begin{aligned} -\delta\Pi \;\; = \;\; & A_1^2 \times (\sqrt{S})^{2\alpha_1+1} H_{11} + A_1 A_2 \times (\sqrt{S})^{\alpha_1+\alpha_2+1}(H_{12}+H_{21}) + A_2^2 \times (\sqrt{S})^{2\alpha_2+1} H_{22} \\ & + A_1 A_3 \times (\sqrt{S})^{\alpha_1+\alpha_3+1} \times (H_{13}+H_{31}) + A_2 A_3 \times (\sqrt{S})^{\alpha_2+\alpha_3+1}(H_{23}+H_{32}) \\ & + A_3^2 \times (\sqrt{S})^{2\alpha_3+1} H_{33} + H.O.T. \end{aligned} \tag{27}$$

Or in concise form:

$$\boxed{-\delta\Pi \approxeq \sum_{i=1}^{3}\sum_{j=1}^{3} A_i\, A_j\, (\sqrt{S})^{\alpha_i+\alpha_j+1}\, H_{ij}} \tag{28}$$

Remark 2. *Note that once* H_{ij} *are available (and can be pre computed and tabulated), then* $\delta\Pi$ *(due to a crack initiation) can be easily computed for any crack surface* S *, at any location along the V-notch edge* z *, having the GESIFs* $A_i(z)$ *of a V-notch without a crack being inserted.*

Remark 3. *The expression in (28) resembles that in 2D [6], with the important distinction that in 2D one has* $\ell^{\alpha_i+\alpha_j}$ *(* ℓ *being the crack length), and in 3D it is* $(\sqrt{S})^{\alpha_i+\alpha_j+1}$

3.2. Computation of H_{ij} *'s*

H_{ij} depend on $\hat{\mathbf{V}}_i$ which can be computed by FE analysis. p-method FE models were constructed for H_{ij} calculation. The relative error in energy norm may be monitored as the p-level is increased in the FE analyses. A numerical integration process (detailed throughout this section) is required for the calculation of H_{ij}, with Gauss quadrature order of 54, and FE models with polynomial degree of 6.

Since $\hat{\mathbf{V}}_i$ is determined in Ω_c^*, a sphere with a radius $\rho^* = R >> 1$ containing a V-notch and a crack located at its center is considered. H_{ij} also depend on ω, the spatial orientation of the crack (θ, φ) and crack shape, and we compute it for crack orientations taken in intervals (or combination of angles φ, θ). An alternative method for H_{ii} calculation is presented in Appendix C.

Because of (16), one needs to apply $\mathcal{T}(\hat{\mathbf{V}}_i) = -\mathcal{T}((\rho^* sin\varphi)^{\alpha_i} \times \boldsymbol{s}_{i0}(\theta))$ on the crack faces Γ_3, Γ_4. Since H_{ij} functions are obtained by a surface intergral over the outer spherical surface of Ω_c^* $(\rho^* \to \infty)$, $\mathcal{T}(\hat{\mathbf{V}}_i)_{\rho^*\to\infty}$ is extracted from the FE model.

For modes I,II and III, a 3D FE model Ω_c^* is used as shown in Fig. 6. Traction free boundary conditions are applied on the V-notch faces. On the crack faces tractions according to (16) are applied as three different sets - for mode I, for mode II, and for mode III, so that the traction vectors are defined individually for each FE model. H_{ij} is computed for each crack inclination angle, and crack shape $(S^* = 1)$.

The outer radius of Ω_c^* was chosen as $\rho^* = R = 100$, large compared to the crack size. Calculations of H_{ij} with different R's between 100 and 400 have shown a negligible influence on the results (less than 2% difference compared with the model with $\rho^* = 100$), indicating that $\rho^* = R = 100$ is large enough. Typically the models contain 13000 tetrahedral elements, resulting in $\sim 1,500,000$ DOF at p=6.

For every choice of angles φ, θ, having ω and the material properties, choosing a crack shape and applying

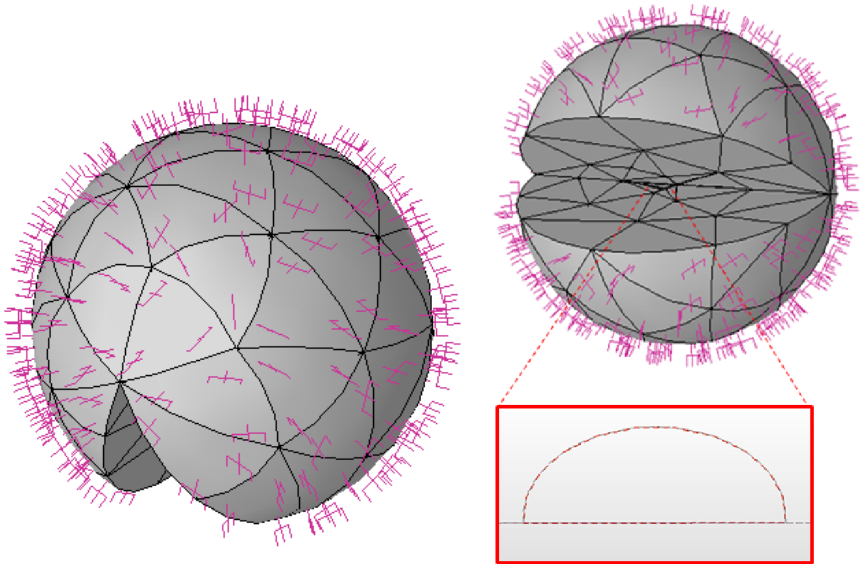

(a) (b)

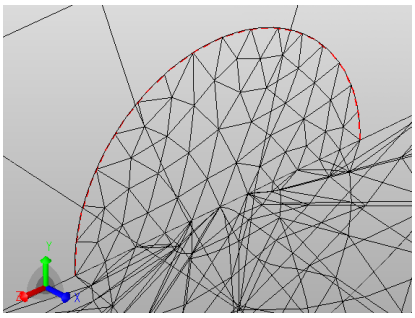

(c)

Figure 6: p-FE models for H_{ij} computation. (a) The FE model of Ω_c^* , (b, c) Zoom-in on the crack at the center of the V-notch tip (crack borders marked in red).

boundary conditions, H_{ij} can be computed by (26) over the outer spherical surface of the domain:

$$\begin{aligned} H_{ij} &= \frac{1}{2}\int_{\frac{\pi-\omega}{2}}^{\frac{\pi+\omega}{2}}\int_{0}^{\pi} \mathcal{T}(\hat{\mathbf{V}}_i) \times (\rho^* \, sin\varphi)^{\alpha_j} \times \boldsymbol{s}_{j0}(\theta) \times (\rho^*)^2 \, sin\varphi \, d\varphi d\theta|_{\rho^*=R} \\ &= \frac{R^{\alpha_j+2}}{2}\int_{\frac{\pi-\omega}{2}}^{\frac{\pi+\omega}{2}}\int_{0}^{\pi} \mathcal{T}(\hat{\mathbf{V}}_i)|_{\rho^*=R}(sin\varphi)^{\alpha_j+1} \times \boldsymbol{s}_{j0}(\theta) \, d\varphi d\theta \end{aligned} \tag{29}$$

$\mathcal{T}(\hat{\mathbf{V}}_i)|_{\rho^*=R} = \left\{ \begin{array}{c} \sigma_{\rho^*\rho^*} \\ \sigma_{\rho^*\varphi} \\ \sigma_{\rho^*\theta} \end{array} \right\}_{\rho^*=R}$ is extracted from the FE solution.

The integrals in (29) are computed numerically using a Gaussian quadrature:

$$H_{ij} = \frac{R^{\alpha_j+2}}{2}\,\frac{\omega}{2}\,\frac{\pi}{2}\sum_{k=1}^{N}\sum_{\ell=1}^{N} W_k W_\ell \left[\mathcal{T}(\hat{\mathbf{V}}_i) \times (sin\varphi_k)^{\alpha_j+1}\, \boldsymbol{s}_{j0}(\theta_\ell)\right] \tag{30}$$

where φ_k, θ_ℓ are the angles associated with the Gaussian quadrature, N is the Gaussian quadrature order, and W_k, W_ℓ are the Gaussian weights. $\boldsymbol{s}_{j0}(\theta)$ is taken from (5), where they are given in cyllindrical coordinates in the "far" domain. $\boldsymbol{s}_{j0}(\theta)$ in (5) are in (r, θ, z) coordinate system:

$$\boldsymbol{s}_{10}(\theta) = \left\{ \begin{array}{c} s_r(\theta) \\ s_\theta(\theta) \\ s_z(\theta) \end{array} \right\}_{10} = \left\{ \begin{array}{c} \left[cos[(1+\alpha_1)(\theta-\frac{\pi}{2})] + \frac{(\lambda+3\mu-\alpha_1(\lambda+\mu))}{(\lambda+\mu)(1-\alpha_1)}\,\frac{sin[\omega(1+\alpha_1)/2]}{sin[\omega(1-\alpha_1)/2]}\,cos[(1-\alpha_1)(\theta-\frac{\pi}{2})]\right]/2\mu\alpha_1 \left(\mathbf{S}_{\theta\theta}(\theta=\frac{\pi}{2})\right)_{10} \\ \left[-sin[(1+\alpha_1)(\theta-\frac{\pi}{2})] - \frac{(\lambda+3\mu+\alpha_1(\lambda+\mu))}{(\lambda+\mu)(1-\alpha_1)}\,\frac{sin[\omega(1+\alpha_1)/2]}{sin[\omega(1-\alpha_1)/2]}\,sin[(1-\alpha_1)(\theta-\frac{\pi}{2})]\right]/2\mu\alpha_1 \left(\mathbf{S}_{\theta\theta}(\theta=\frac{\pi}{2})\right)_{10} \\ 0 \end{array} \right\}$$

$$\boldsymbol{s}_{20}(\theta) = \left\{ \begin{array}{c} s_r(\theta) \\ s_\theta(\theta) \\ s_z(\theta) \end{array} \right\}_{20} = \left\{ \begin{array}{c} \left[sin[(1+\alpha_2)(\theta-\frac{\pi}{2})] + \frac{(\lambda+3\mu-\alpha_2(\lambda+\mu))}{(\lambda+\mu)(1+\alpha_2)}\,\frac{sin[\omega(1+\alpha_2)/2]}{sin[\omega(1-\alpha_2)/2]}\,sin[(1-\alpha_2)(\theta-\frac{\pi}{2})]\right]/2\mu\alpha_2 \left(\mathbf{S}_{r\theta}(\theta=\frac{\pi}{2})\right)_{20} \\ \left[cos[(1+\alpha_2)(\theta-\frac{\pi}{2})] + \frac{(\lambda+3\mu+\alpha_2(\lambda+\mu))}{(\lambda+\mu)(1+\alpha_2)}\,\frac{sin[\omega(1+\alpha_2)/2]}{sin[\omega(1-\alpha_2)/2]}\,cos[(1-\alpha_2)(\theta-\frac{\pi}{2})]\right]/2\mu\alpha_2 \left(\mathbf{S}_{r\theta}(\theta=\frac{\pi}{2})\right)_{20} \\ 0 \end{array} \right\}$$

$$\boldsymbol{s}_{30}(\theta) = \left\{ \begin{array}{c} s_r(\theta) \\ s_\theta(\theta) \\ s_z(\theta) \end{array} \right\}_{30} = \left\{ \begin{array}{c} 0 \\ 0 \\ \frac{\omega}{\pi\mu}\,sin[\frac{\pi}{\omega}(\theta-\frac{\pi}{2})] \end{array} \right\} \tag{31}$$

Therefore a transformation from cylindrical to spherical coordinates is performed:

$$\left\{ \begin{array}{c} s_{\rho^*}(\theta) \\ s_\varphi(\theta) \\ s_\theta(\theta) \end{array} \right\}_{i0} = \left(\begin{array}{ccc} sin\varphi & 0 & cos\varphi \\ cos\varphi & 0 & -sin\varphi \\ 0 & 1 & 0 \end{array} \right) \left\{ \begin{array}{c} s_{r^*}(\theta) \\ s_\theta(\theta) \\ s_z(\theta) \end{array} \right\}_{i0} \tag{32}$$

Substituting (32) in (30) one obtains:

$$\begin{array}{l} \mathcal{T}(\hat{\mathbf{V}}_i) \times (sin\varphi)^{\alpha_j+1}\, \boldsymbol{s}_{j0}(\theta) = \\ \quad (sin\varphi)^{\alpha_j+1} \left[(\sigma_{\rho^*\rho^*})_{FE\,i} \times (\boldsymbol{s}_{\rho^*}(\theta))_{j0} + (\sigma_{\rho^*\varphi})_{FE\,i} \times (\boldsymbol{s}_\varphi(\theta))_{j0} + (\sigma_{\rho^*\theta})_{FE\,i} \times (\boldsymbol{s}_\theta(\theta))_{j0}\right]_{\rho^*=R} \end{array} \tag{33}$$

where $(\sigma_{\rho^*\rho^*})_{FE\,i}$, $(\sigma_{\rho^*\varphi})_{FE\,i}$, $(\sigma_{\rho^*\theta})_{FE\,i}$ are FE stresses on $\rho^* = R$ resulting from BCs on crack faces associated with mode i ($i = 1, 2,$ or 3). Finally (30) in an explicit form is:

$$
\begin{aligned}
H_{11} &= \frac{R^{\alpha_1+2}}{2}\frac{2\pi-\omega}{2}\frac{\pi}{2}\sum_{k=1}^{N}\sum_{\ell=1}^{N}W_kW_\ell\left\{(sin\varphi_k)^{\alpha_1+1}\times\left[\left(\sigma_{\rho^*\rho^*}\right)_{FE\,1}\left(\boldsymbol{s}_{\rho^*}(\theta_\ell)\right)_{10}+\left(\sigma_{\rho^*\varphi}\right)_{FE\,1}\left(\boldsymbol{s}_{\varphi}(\theta_\ell)\right)_{10}+\left(\sigma_{\rho^*\theta}\right)_{FE\,1}\left(\boldsymbol{s}_{\theta}(\theta_\ell)\right)_{10}\right]\right\}_{\rho^*=R}\\
H_{12} &= \frac{R^{\alpha_2+2}}{2}\frac{2\pi-\omega}{2}\frac{\pi}{2}\sum_{k=1}^{N}\sum_{\ell=1}^{N}W_kW_\ell\left\{(sin\varphi_k)^{\alpha_2+1}\times\left[\left(\sigma_{\rho^*\rho^*}\right)_{FE\,1}\left(\boldsymbol{s}_{\rho^*}(\theta_\ell)\right)_{20}+\left(\sigma_{\rho^*\varphi}\right)_{FE\,1}\left(\boldsymbol{s}_{\varphi}(\theta_\ell)\right)_{20}+\left(\sigma_{\rho^*\theta}\right)_{FE\,1}\left(\boldsymbol{s}_{\theta}(\theta_\ell)\right)_{20}\right]\right\}_{\rho^*=R}\\
H_{13} &= \frac{R^{\alpha_3+2}}{2}\frac{2\pi-\omega}{2}\frac{\pi}{2}\sum_{k=1}^{N}\sum_{\ell=1}^{N}W_kW_\ell\left\{(sin\varphi_k)^{\alpha_3+1}\times\left[\left(\sigma_{\rho^*\rho^*}\right)_{FE\,1}\left(\boldsymbol{s}_{\rho^*}(\theta_\ell)\right)_{30}+\left(\sigma_{\rho^*\varphi}\right)_{FE\,1}\left(\boldsymbol{s}_{\varphi}(\theta_\ell)\right)_{30}+\left(\sigma_{\rho^*\theta}\right)_{FE\,1}\left(\boldsymbol{s}_{\theta}(\theta_\ell)\right)_{30}\right]\right\}_{\rho^*=R}\\
H_{21} &= \frac{R^{\alpha_1+2}}{2}\frac{2\pi-\omega}{2}\frac{\pi}{2}\sum_{k=1}^{N}\sum_{\ell=1}^{N}W_kW_\ell\left\{(sin\varphi_k)^{\alpha_1+1}\times\left[\left(\sigma_{\rho^*\rho^*}\right)_{FE\,2}\left(\boldsymbol{s}_{\rho^*}(\theta_\ell)\right)_{10}+\left(\sigma_{\rho^*\varphi}\right)_{FE\,2}\left(\boldsymbol{s}_{\varphi}(\theta_\ell)\right)_{10}+\left(\sigma_{\rho^*\theta}\right)_{FE\,2}\left(\boldsymbol{s}_{\theta}(\theta_\ell)\right)_{10}\right]\right\}_{\rho^*=R}\\
H_{22} &= \frac{R^{\alpha_2+2}}{2}\frac{2\pi-\omega}{2}\frac{\pi}{2}\sum_{k=1}^{N}\sum_{\ell=1}^{N}W_kW_\ell\left\{(sin\varphi_k)^{\alpha_2+1}\times\left[\left(\sigma_{\rho^*\rho^*}\right)_{FE\,2}\left(\boldsymbol{s}_{\rho^*}(\theta_\ell)\right)_{20}+\left(\sigma_{\rho^*\varphi}\right)_{FE\,2}\left(\boldsymbol{s}_{\varphi}(\theta_\ell)\right)_{20}+\left(\sigma_{\rho^*\theta}\right)_{FE\,2}\left(\boldsymbol{s}_{\theta}(\theta_\ell)\right)_{20}\right]\right\}_{\rho^*=R}\\
H_{23} &= \frac{R^{\alpha_3+2}}{2}\frac{2\pi-\omega}{2}\frac{\pi}{2}\sum_{k=1}^{N}\sum_{\ell=1}^{N}W_kW_\ell\left\{(sin\varphi_k)^{\alpha_3+1}\times\left[\left(\sigma_{\rho^*\rho^*}\right)_{FE\,2}\left(\boldsymbol{s}_{\rho^*}(\theta_\ell)\right)_{30}+\left(\sigma_{\rho^*\varphi}\right)_{FE\,2}\left(\boldsymbol{s}_{\varphi}(\theta_\ell)\right)_{30}+\left(\sigma_{\rho^*\theta}\right)_{FE\,2}\left(\boldsymbol{s}_{\theta}(\theta_\ell)\right)_{30}\right]\right\}_{\rho^*=R}\\
H_{31} &= \frac{R^{\alpha_1+2}}{2}\frac{2\pi-\omega}{2}\frac{\pi}{2}\sum_{k=1}^{N}\sum_{\ell=1}^{N}W_kW_\ell\left\{(sin\varphi_k)^{\alpha_1+1}\times\left[\left(\sigma_{\rho^*\rho^*}\right)_{FE\,3}\left(\boldsymbol{s}_{\rho^*}(\theta_\ell)\right)_{10}+\left(\sigma_{\rho^*\varphi}\right)_{FE\,3}\left(\boldsymbol{s}_{\varphi}(\theta_\ell)\right)_{10}+\left(\sigma_{\rho^*\theta}\right)_{FE\,3}\left(\boldsymbol{s}_{\theta}(\theta_\ell)\right)_{10}\right]\right\}_{\rho^*=R}\\
H_{32} &= \frac{R^{\alpha_2+2}}{2}\frac{2\pi-\omega}{2}\frac{\pi}{2}\sum_{k=1}^{N}\sum_{\ell=1}^{N}W_kW_\ell\left\{(sin\varphi_k)^{\alpha_2+1}\times\left[\left(\sigma_{\rho^*\rho^*}\right)_{FE\,3}\left(\boldsymbol{s}_{\rho^*}(\theta_\ell)\right)_{20}+\left(\sigma_{\rho^*\varphi}\right)_{FE\,3}\left(\boldsymbol{s}_{\varphi}(\theta_\ell)\right)_{20}+\left(\sigma_{\rho^*\theta}\right)_{FE\,3}\left(\boldsymbol{s}_{\theta}(\theta_\ell)\right)_{20}\right]\right\}_{\rho^*=R}\\
H_{33} &= \frac{R^{\alpha_3+2}}{2}\frac{2\pi-\omega}{2}\frac{\pi}{2}\sum_{k=1}^{N}\sum_{\ell=1}^{N}W_kW_\ell\left\{(sin\varphi_k)^{\alpha_3+1}\times\left[\left(\sigma_{\rho^*\rho^*}\right)_{FE\,3}\left(\boldsymbol{s}_{\rho^*}(\theta_\ell)\right)_{30}+\left(\sigma_{\rho^*\varphi}\right)_{FE\,3}\left(\boldsymbol{s}_{\varphi}(\theta_\ell)\right)_{30}+\left(\sigma_{\rho^*\theta}\right)_{FE\,3}\left(\boldsymbol{s}_{\theta}(\theta_\ell)\right)_{30}\right]\right\}_{\rho^*=R}
\end{aligned}
\tag{34}
$$

Remark 4. *It seems as if H_{ij} in (34) tend to infinity since $R\to\infty$. However, since $\sigma_{ij}\to 0$ we obtain $H_{ij}\to const.$ H_{ij} were calculated for R between 100 and 400 and the influence of R on the results was negligible - H_{ij} approaches a constant value, therefore $R=100$ is already large enough to "represent infinity".*

4. On the accuracy of the asymptotic estimation of $\delta\Pi$

To verify the accuracy of $\delta\Pi$ obtained by the asymptotic expansion, we consider a rectangular bar with a V-notch as shown in Fig. 10. We compute the potential energy twice, with and without a crack located at the V-notch edge. The difference in the potential energy is: $\delta\Pi^{FE}=\Pi^{FE}_{V-notch+crack}-\Pi^{FE}_{V-notch}$ (see Fig. 2). For both FE models, the V-notch angle is $\omega=315^\circ$, perpendicular to the specimen facet. For the models containing a crack, the crack intersected the V-notch at its middle ($z_0=5mm$). The specimen was given material properties of PMMA: $E=3900\,MPa$, $\nu=0.332$. $\delta\Pi$ is also computed by the asymptotic expression (28).

4.1. Numerical evaluation of H_{ij}

H_{ij} 's have been computed in a spherical FE model with an outer radius of $\rho^*=R=100$ (see Fig. 6). Several crack orientations and shapes were considered: a half-circular crack along (100) plane, which can be represented as $\varphi=90^o,\theta=0^o$, and (-110) plane, where $\varphi=90^o,\theta=135^o$, and also a half elliptical crack (Fig. 8) with $a/b=2$ ratio (see Fig. 13 for notations) along the (100) plane and $(-\sqrt{3}10)$ plane, where $\varphi=90^o,\theta=150^o$. θ represents the angle between the normal to the plane and the x axis. Circular cracks along the (-101) , (111) , (212) and $(51(-3))$ planes were also considered. The H_{ij} values obtained for these geometries are presented in Tables 1 and 2. Schematic representations of the crack orientations are shown in Fig. 7 and 9.

crack orientation	(100)	(-110)	(100)	$(-\sqrt{3}10)$
crack shape a/b	circular 1	circular 1	ellipse 2	ellipse 2
H_{11}	$8.45 \cdot 10^{-4}$	$6.25 \cdot 10^{-4}$	$1.04 \cdot 10^{-3}$	$9.13 \cdot 10^{-4}$
H_{12}	$-8.52 \cdot 10^{-8}$	$3.8 \cdot 10^{-4}$	$1.25 \cdot 10^{-7}$	$3.51 \cdot 10^{-4}$
H_{13}	$-4.67 \cdot 10^{-8}$	$-2.22 \cdot 10^{-7}$	$1.22 \cdot 10^{-7}$	$7.08 \cdot 10^{-8}$
H_{21}	$1.24 \cdot 10^{-8}$	$3.8 \cdot 10^{-4}$	$8.2 \cdot 10^{-8}$	$3.54 \cdot 10^{-4}$
H_{22}	$5.32 \cdot 10^{-4}$	$5.85 \cdot 10^{-4}$	$5.53 \cdot 10^{-4}$	$6.19 \cdot 10^{-4}$
H_{23}	$-1.32 \cdot 10^{-7}$	$-2.8 \cdot 10^{-6}$	$6.13 \cdot 10^{-8}$	$-1.62 \cdot 10^{-7}$
H_{31}	$1.61 \cdot 10^{-8}$	$-3.53 \cdot 10^{-7}$	$5.72 \cdot 10^{-8}$	$4.65 \cdot 10^{-8}$
H_{32}	$2.85 \cdot 10^{-7}$	$-2.56 \cdot 10^{-6}$	$1.89 \cdot 10^{-7}$	$-4 \cdot 10^{-7}$
H_{33}	$7.98 \cdot 10^{-4}$	$6.52 \cdot 10^{-4}$	$1.02 \cdot 10^{-3}$	$9.49 \cdot 10^{-4}$

Table 1: H_{ij} at different orientations ($E = 3900\,MPa$, $\nu = 0.332$), $\omega = 315°$ as in Fig. 7

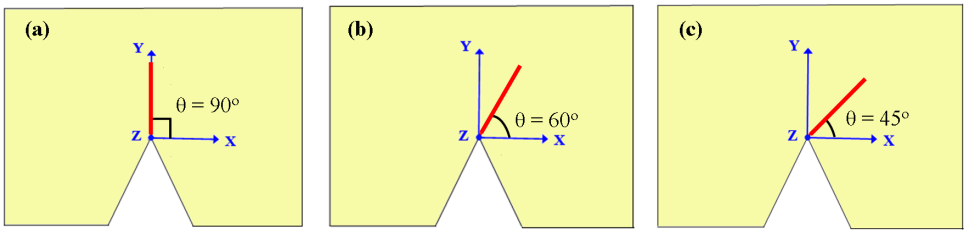

Figure 7: Schematic representation of models containing cracks (in red) along (a) (100) (b) $(-\sqrt{3}10)$ (c) (-110) .

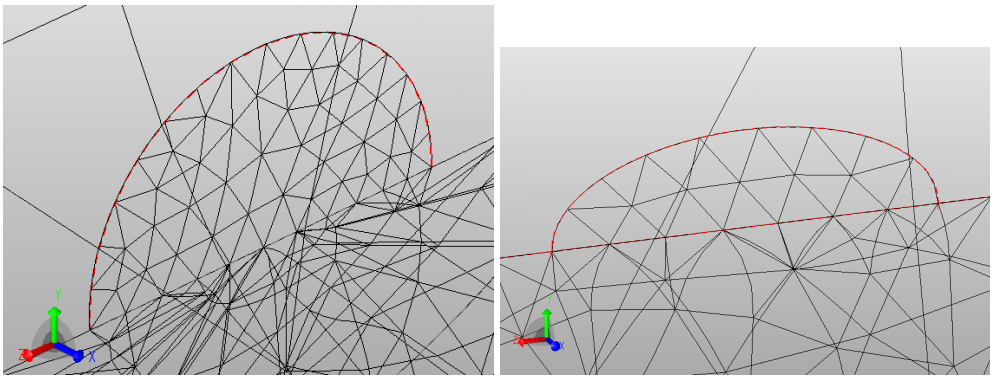

(a) (b)

Figure 8: Zoom-in on the (a) half-circular and (b) half-elliptical cracks area in the FE models. The cracks edge is marked in red.

4.2. Numerical evaluation of $\delta\Pi$

To compute $\delta\Pi$, $A_i(z)$ for the V-notch edge with no crack must be computed. These were computed by the Quasi-Dual Function Method [9], using a FE model having refinements arround the V-notch edge (see Fig. 10). Having H_{ij} , A_i and the crack area from the respective bar-shaped model (eigenvalues α_i are known), $\delta\Pi^{Approx}$ is computed by (28).

crack orientation	(-101)	(111)	(212)	$(51(-3))$
crack shape a/b	circular 1	circular 1	circular 1	circular 1
H_{11}	$2.73 \cdot 10^{-4}$	$2.28 \cdot 10^{-4}$	$2.59 \cdot 10^{-4}$	$3.82 \cdot 10^{-4}$
H_{12}	$1.05 \cdot 10^{-8}$	$-1.37 \cdot 10^{-4}$	$-9.32 \cdot 10^{-5}$	$-6.29 \cdot 10^{-5}$
H_{13}	$2.65 \cdot 10^{-4}$	$-1.71 \cdot 10^{-4}$	$-2.34 \cdot 10^{-4}$	$2.52 \cdot 10^{-4}$
H_{21}	$7.76 \cdot 10^{-9}$	$-1.36 \cdot 10^{-4}$	$-8.45 \cdot 10^{-5}$	$-6.22 \cdot 10^{-5}$
H_{22}	$1.23 \cdot 10^{-4}$	$1.76 \cdot 10^{-4}$	$1.18 \cdot 10^{-4}$	$1.92 \cdot 10^{-4}$
H_{23}	$8.21 \cdot 10^{-8}$	$1.15 \cdot 10^{-4}$	$6.75 \cdot 10^{-5}$	$-1.76 \cdot 10^{-5}$
H_{31}	$2.64 \cdot 10^{-4}$	$-1.7 \cdot 10^{-4}$	$-2.32 \cdot 10^{-4}$	$2.5 \cdot 10^{-4}$
H_{32}	$-2.66 \cdot 10^{-8}$	$1.15 \cdot 10^{-4}$	$7.12 \cdot 10^{-5}$	$-1.78 \cdot 10^{-5}$
H_{33}	$3.15 \cdot 10^{-4}$	$2.44 \cdot 10^{-4}$	$2.96 \cdot 10^{-4}$	$3.37 \cdot 10^{-4}$

Table 2: H_{ij} at different orientations ($E = 3900\,MPa$, $\nu = 0.332$), $\omega = 315^\circ$ as in Fig. 9.

4.2.1. $\delta\Pi$ for mode I loading

Out of several configurations considered under mode I loading, we provide a representative example: a FE model $10 \times 5 \times 10\,mm$ under tension is shown in Fig. 10. An auto-mesher was used, and various FE meshes have been examined to reduce the numerical errors of the models. The mesh was refined around the V-notch edge, crack, loading and support regions. Tension boundary conditions ($100\,MPa$) were applied along the x direction. The crack shape was half a circle, located in the center of the V-notch edge, with orientation along the (100) plane. Both FE models (V-notched with and without a crack) were identically meshed, so that the crack was defined as two separate surfaces and in the V-notched model without the crack the surfaces were merged. The two identical meshes ensure that the numerical errors associated with mesh away from the crack cancel each other when computing

$$\delta\Pi^{FE} \triangleq \Pi^{FE}_{V-notch+crack} - \Pi^{FE}_{V-notch} \tag{35}$$

$A_1(z)$ along the V-notch edge $(0 \le z \le 10\,mm)$ was extracted by the QDFM and presented graphically in Fig. 10 $(A_2(z) = A_3(z) = 0)$. The crack is located at the middle of the V-notch edge so we used $A_1(z_0 = 5)$ to compute $\delta\Pi^{Approx}$ by (28). Several crack radii between $0.01 - 0.1\,mm^2$ were examined. Cracks with areas larger than $0.1\,mm^2$ - compared to the 10 mm long V-notch edge - are probably inadequate for the $\delta\Pi$ calculation as they are not "small" enough. Potential energy, $\delta\Pi^{FE}$, and $\delta\Pi^{Approx}$ results for this geometry are presented in Table 3.

One may notice that for all crack areas the difference between $\delta\Pi^{FE}$ and $\delta\Pi^{Approx}$ is under 5%. For other bar-shaped geometries examined under tension, such as $16\times5\times10\,mm$ (which are not presented in this article), the difference between $\delta\Pi^{FE}$ and $\delta\Pi^{Approx}$ was under 8%. The difference in the results is attributed to the numerical errors in $\delta\Pi^{FE}$, numerical errors in the computation of H_{ij} and $A_i(z)$, and of course $\delta\Pi^{Approx}$ is a better approximation as $\delta S \to 0$.

To ensure the accuracy of $\delta\Pi^{FE}$, we also computed by the h-FEA program ABAQUS, obtaining similar results. In spite of attempts to obtain accurate $\delta\Pi^{FE}$, the error is hard to evaluate, and it is difficult to further increase the accuracy of the results. The numerical errors from both the bar-shaped models and the spherical models for $\delta\Pi^{Approx}$ calculation contribute to the overall relative error. The ratio $\frac{\delta\Pi^{FE}}{\Pi^{FE}}$ is very small for all geometries tested, as can be seen in Table 3: $\frac{\delta\Pi^{FE}}{\Pi^{FE}} \sim 0.0019$ for $S = 0.1$ and $\frac{\delta\Pi^{FE}}{\Pi^{FE}} \sim 0.00018$ for $S = 0.01$, whereas the error in energy norm of the FE models is about 3%.

Nevertheless, the small difference between $\delta\Pi^{FE}$ and $\delta\Pi^{Approx}$ indicates that $\delta\Pi^{Approx}$ is an accurate estimation.

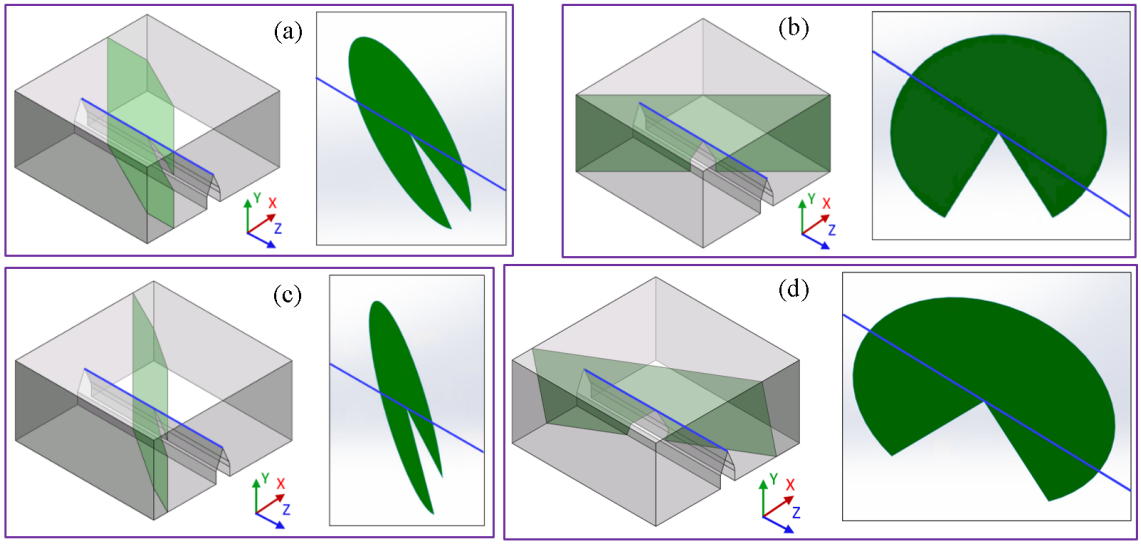

Figure 9: The planes: (a) (111) , (b) (-101) , (c) (212) and (d) $(51(-3))$ within a $10 \times 5 \times 10\, mm$ geometry, and circular cracks along the same planes. The V-notch edge (z axis) is represented by the blue line.

4.2.2. $\delta\Pi$ for mixed mode (I+II+III) loading

$\delta\Pi$ under mixed-mode conditions (modes I+II+III) was computed for the same bar as in section 4.2.1 with different boundary conditions (Fig. 11). The left face was clamped whereas on the opposite face tractions of $1000\, MPa$ were applied in directions $x, y,$ and z . Several crack orientations, shapes and sizes were examined as shown in Table 4. The cracks were located at the center of the V-notch edge in all cases $(z_0 = 5)$. $\delta\Pi^{FE}$ results from several FE models (for polynomial degree of p=6 and ~ 850000 DOF) and respective $\delta\Pi^{Approx}$ computed by (28) are presented in Table 4 with H_{ij} values presented in Table 1 and $A_i(z)$ extracted by the QDFM are shown in Fig. 12. Schematic representation of the crack orientations are shown in Fig. 7 and 9.

The difference between $\delta\Pi^{Approx}$ and $\delta\Pi^{FE}$ for the mixed mode loading is less than 9% for all crack orientations shapes and sizes presented in Table 4. Together with the previous results (Table 3), we have obtained less than 9% error between $\delta\Pi^{Approx}$ and $\delta\Pi^{FE}$ results for a variety of boundary conditions, cracks shapes, sizes and orientations.

We can conclude, that the small difference of $\delta\Pi^{Approx}$ compared to $\delta\Pi^{FE}$ throughout this section reassures the correctness of the asymptotic analysis presented in Chapter 3.

4.3. Crack shape influence on the H_{ij} 's

H_{ij} depends on the crack shape (in addition to dependence on the orientation, V-notch solid angle ω and mechanical properties). We examine the sensitivity to crack shape, by considering half ellipses with an area of 1 with different major to minor radii ratios - see Figs. 13 and 8. The crack orientation was along the V-notch bisector (100), and a/b between 10 and 0.1. H_{ii} results were obtained by both methods described in Appendix C, and are presented in Table 5. The H_{ij} results computed by (34) are denoted by H_{ij} and obtained for polynomial degree $p = 6$ and 54 integration points. The results using Appendix C for a polynomial degree of $p = 6$ are presented for H_{ii} and denoted by $H_{ii}^{\Omega^*}$. A graphical representation of the H_{11} and H_{33} as a function of a/b is presented in Fig. 14.

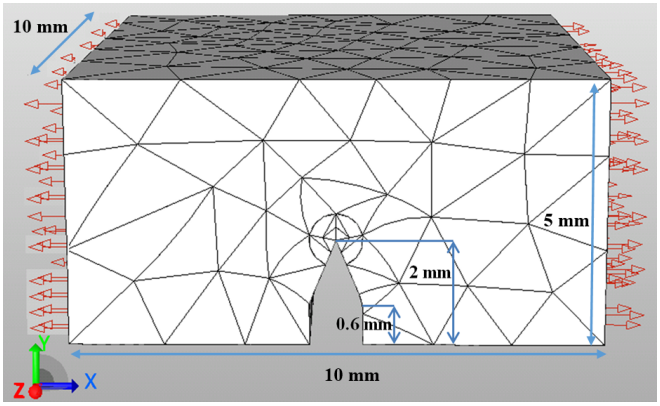

(a)

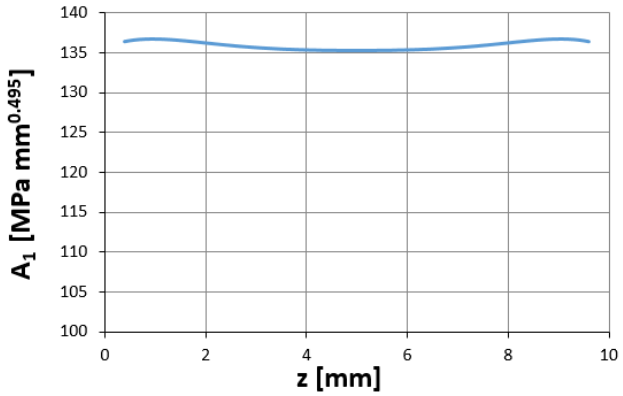

(b)

Figure 10: (a) A FE model of a $10 \times 5 \times 10\,mm$ bar with a V-notch and (b) the respective $A_1(z)$ along the V-notch edge

One may observe that the crack shape influences the H_{ij} results significantly (between $a/b = 0.1$ and $a/b = 10$ there is a difference of an order of magnitude in H_{ij}).

Fig. 14 presents monotonic increase in H_{11} values. As a result, $\delta\Pi$ values will increase monotonically as well, as a/b increases. This behavior is expected since a larger a/b means that a larger portion of the unit area crack is close to the V-notch edge and therefore the contribution of this cracks formation to the potential energy difference is larger.

The difference between H_{ij} and $H_{ij}^{\Omega^*}$ is under 3%. Appendix C elaborates on the additional method for H_{ii} calculation.

In [6] the relation between 2D H_{ij} functions for different E [MPa] and ν values was introduced:

$$H_{ij}^{new}(\omega,\theta) = H_{ij}(\omega,\theta)\,\frac{E}{1-\nu^2}\,\frac{1-(\nu^{new})^2}{E^{new}} \tag{36}$$

This relation was examined for the 3D H_{ij} functions. Two spherical models for H_{ij} calculation with different crack orientation and shape were given combinations of material properties within a wide range: $1 \le E \le 10^4\,[MPa]$, $0 \le \nu \le 0.4$. The H_{ij} values for models with different E, ν were compared with those calculated by (36) with $E = 1[MPa]$, $\nu = 0.3$ as reference properties. H_{ij} depends linearly on E , but not so for ν and (36) is incorrect with respect to ν in 3D.

crack orientation	crack area $[mm^2]$	Π^{FE} $p \to \infty$ $[N \cdot mm]$	FE error in energy norm at p=7	$\delta\Pi^{FE}$ $[N \cdot mm]$ from FE models	$\delta\Pi^{Approx}$ $[N \cdot mm]$	% difference between $\delta\Pi^{FE}$ and $\delta\Pi^{Approx}$
no crack		-840.83	2.56%	-1.609	-1.53	4.89%
(100)	0.1	-842.43	2.61%			
no crack		-840.74	2.76%	-1.12	-1.07	4.53%
(100)	0.07	-841.86	2.79%			
no crack		-840.73	2.73%	-0.798	-0.762	4.4%
(100)	0.05	-841.53	2.74%			
no crack		-840.73	2.65%	-0.476	-0.456	4.14%
(100)	0.03	-841.21	2.66%			
no crack		-840.74	2.81%	-0.157	-0.151	3.7%
(100)	0.01	-840.9	2.82%			

Table 3: $\delta\Pi^{FE}$ results compared to $\delta\Pi^{Approx}$ for the $10 \times 5 \times 10\,mm$ V-notched geometry.

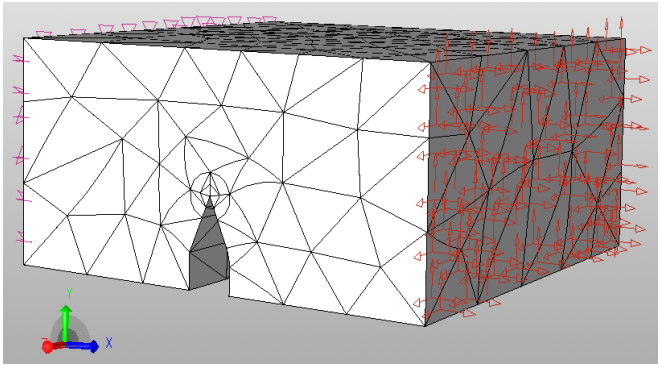

Figure 11: FE model for the mixed mode computations.

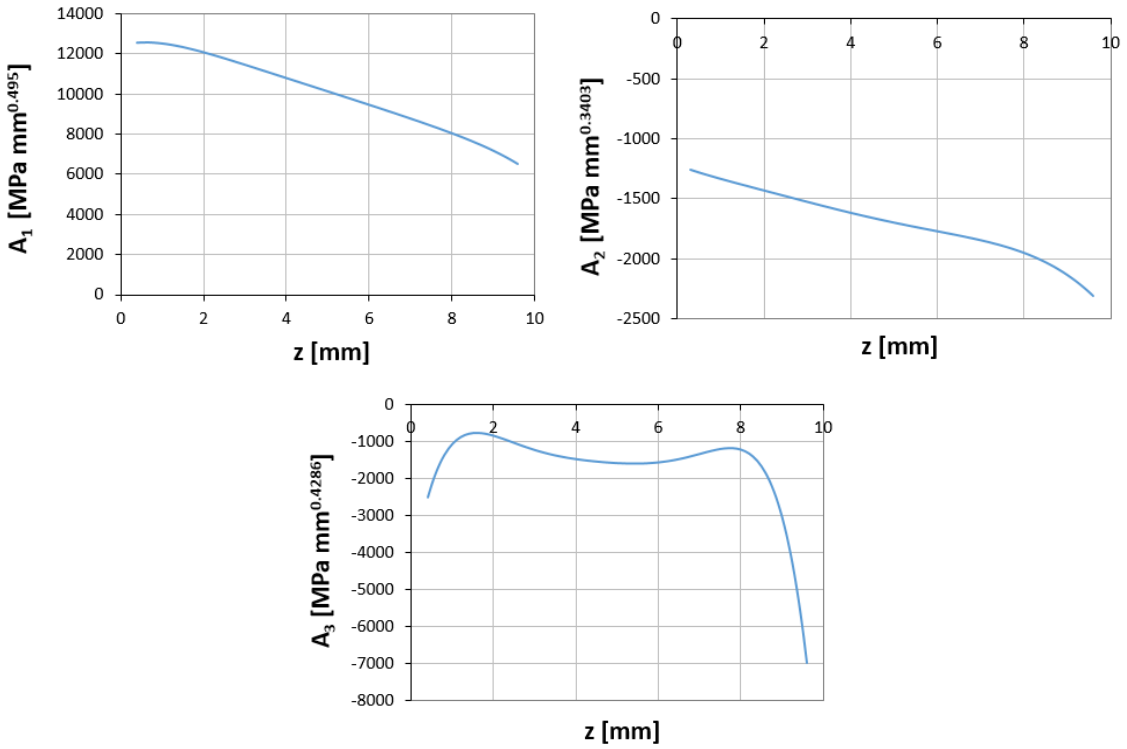

Figure 12: $A_1(z)$, $A_2(z)$, and $A_3(z)$ for a $10 \times 5 \times 10\,mm$ bar with a V-notch of $\omega = 315°$ under mixed mode loading.

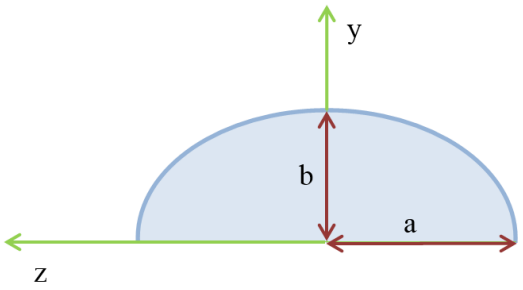

Figure 13: Ellipse notations

crack orientation	crack shape: a/b of ellipse	crack area $[mm^2]$	Π^{FE} $p \to \infty [N \cdot mm]$	FE error in energy norm at p=7	$\delta\Pi^{FE}$ $[N \cdot mm]$ from FE models	$\delta\Pi^{Approx}$ $[N \cdot mm]$	% difference between $\delta\Pi^{FE}$ and $\delta\Pi^{Approx}$
no crack			-2828702	3.57%	-8910	-8723	2.1%
(100)	1	0.1	-2837612	3.63%			
no crack			-2828727	3.6%	-11267	-10972	2.35%
(100)	2	0.1	-2839964	3.64%			
no crack			-2828645	3.86%	-4488	-4325	3.63%
$(-\sqrt{3}10)$	2	0.05	-2833133	3.86%			
no crack			-2828674	3.93%	-2924	-2786	4.7%
(-110)	1	0.05	-2831598	3.93%			
no crack			-2828667	3.85%	-944	-1027	-8.9%
(-101)	1	0.05	-2829608	3.86%			
no crack			-2828677	3.7%	-3537	-3261	7.8%
(111)	1	0.1	-2832214	3.75%			
no crack			-2828656	3.6%	-3906	-3758	3.8%
(212)	1	0.1	-2832563	3.62%			
no crack			-2828699	3.84%	-1628	-1691	-3.9%
$(51-3)$	1	0.05	-2830327	3.85%			

Table 4: $\delta\Pi^{FE}$ results compared to $\delta\Pi^{Approx}$ for the $10 \times 5 \times 10\, mm$ models under mixed mode (I+II+III) loading

a/b	10	5	2	1	0.5	0.1
H_{11}	$1.21 \cdot 10^{-3}$	$1.17 \cdot 10^{-3}$	$1.04 \cdot 10^{-3}$	$8.45 \cdot 10^{-4}$	$6.05 \cdot 10^{-4}$	$1.94 \cdot 10^{-4}$
$H_{11}^{\Omega^*}$	$1.17 \cdot 10^{-3}$	$1.14 \cdot 10^{-3}$	$1.03 \cdot 10^{-3}$	$8.42 \cdot 10^{-4}$	$6.03 \cdot 10^{-4}$	$1.94 \cdot 10^{-4}$
H_{12}	$5.85 \cdot 10^{-6}$	$-1.64 \cdot 10^{-6}$	$1.25 \cdot 10^{-7}$	$-8.52 \cdot 10^{-8}$	$-3.24 \cdot 10^{-7}$	$-4.03 \cdot 10^{-8}$
H_{13}	$2.44 \cdot 10^{-7}$	$7.93 \cdot 10^{-8}$	$1.22 \cdot 10^{-7}$	$-4.67 \cdot 10^{-8}$	$-2 \cdot 10^{-7}$	$6.44 \cdot 10^{-8}$
H_{21}	$5.73 \cdot 10^{-6}$	$-1.38 \cdot 10^{-6}$	$8.2 \cdot 10^{-8}$	$1.24 \cdot 10^{-8}$	$1.78 \cdot 10^{-7}$	$-4.5 \cdot 10^{-8}$
H_{22}	$4.53 \cdot 10^{-4}$	$5.07 \cdot 10^{-4}$	$5.53 \cdot 10^{-4}$	$5.32 \cdot 10^{-4}$	$4.39 \cdot 10^{-4}$	$1.73 \cdot 10^{-4}$
$H_{22}^{\Omega^*}$	$4.48 \cdot 10^{-4}$	$5.03 \cdot 10^{-4}$	$5.51 \cdot 10^{-4}$	$5.34 \cdot 10^{-4}$	$4.4 \cdot 10^{-4}$	$1.73 \cdot 10^{-4}$
H_{23}	$4.97 \cdot 10^{-8}$	$3.09 \cdot 10^{-8}$	$6.13 \cdot 10^{-8}$	$-1.32 \cdot 10^{-7}$	$2.48 \cdot 10^{-7}$	$-1.05 \cdot 10^{-7}$
H_{31}	$5.34 \cdot 10^{-7}$	$-1.35 \cdot 10^{-7}$	$5.72 \cdot 10^{-8}$	$1.61 \cdot 10^{-8}$	$-1.51 \cdot 10^{-7}$	$7 \cdot 10^{-8}$
H_{32}	$1.85 \cdot 10^{-7}$	$6.63 \cdot 10^{-7}$	$1.89 \cdot 10^{-7}$	$2.85 \cdot 10^{-7}$	$2.3 \cdot 10^{-7}$	$-1.27 \cdot 10^{-7}$
H_{33}	$1.16 \cdot 10^{-3}$	$1.15 \cdot 10^{-3}$	$1.02 \cdot 10^{-3}$	$7.98 \cdot 10^{-4}$	$5.43 \cdot 10^{-4}$	$1.63 \cdot 10^{-4}$
$H_{33}^{\Omega^*}$	$1.13 \cdot 10^{-3}$	$1.13 \cdot 10^{-3}$	$1.01 \cdot 10^{-3}$	$7.95 \cdot 10^{-4}$	$5.43 \cdot 10^{-4}$	$1.62 \cdot 10^{-4}$

Table 5: H_{ij} values for elliptical cracks (100) and different a/b ratios.

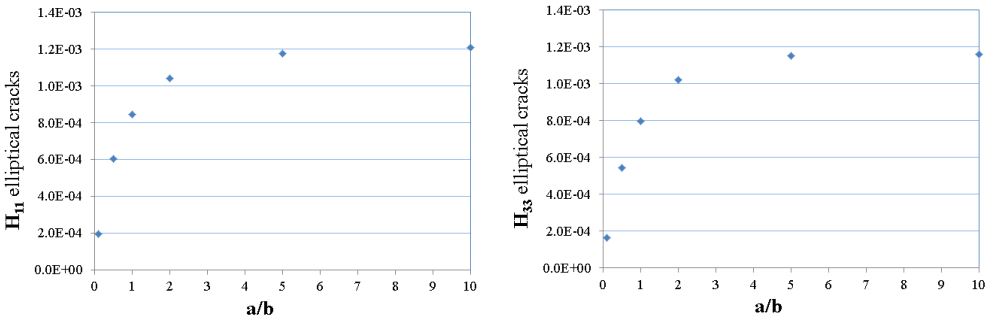

(a) (b)

Figure 14: Graphical representation of the H_{11} (a) and H_{33} (b) for elliptical cracks on plane (100) and different a/b ratios.

5. Summary and conclusions

We have derived an explicit expression for $\delta\Pi$, the difference in the potential energy between a V-notch with and without a small crack initiating at its edge in a 3D elastic domain under a general mixed mode I+II+III loading. $\delta\Pi$ depends on numerous variables - crack shape, size, orientation, far boundary conditions ($A_i(z)$), V-notch solid angle (ω) and material properties. The functions H_{ij} are independent of crack size and far boundary conditions, so only one calculation of H_{ij} is needed (for a chosen crack orientation and shape) in order to obtain $\delta\Pi$ for all crack sizes and sets of far boundary conditions. The values approximated by the asymptotic expansion ($\delta\Pi^{Approx}$) were verified by comparison to values obtained from two FE models of a chosen bar-shaped geometry ($\delta\Pi^{FE}$), with and without a crack initiating from the V-notch. Calculation by the $\delta\Pi^{FE}$ method is impractical since it would compel the construction of two FE models (with and without a crack) for each crack size, location and set of far boundary conditions separately, as opposed to $\delta\Pi^{Approx}$, which can be easily computed for any crack size, location and set of far boundary conditions once H_{ij} are available (and can be pre-computed and tabulated), and the GESIFs $A_i(z)$ of a V-notch without a crack are known. In addition, the ratio $\frac{\delta\Pi^{FE}}{\Pi^{FE}}$ was shown to be very small for all geometries tested (Table 3: $\frac{\delta\Pi^{FE}}{\Pi^{FE}} < 0.002$, whereas the error in energy norm of the FE models is about 3%), which may weaken the reliability of the results, especially for very small cracks. The H_{ij} calculation, on the other hand, involves numerical integration, which contributes to decreasing the numerical error. Nevertheless, the difference between $\delta\Pi^{FE}$ and $\delta\Pi^{Approx}$ was small (for a variety of boundary conditions, cracks shapes, sizes and orientations) which indicates that $\delta\Pi^{Approx}$ is an accurate estimation.

A crack shape must be determined to perform a 3D analysis. We have demonstrated that this parameter influences H_{ij} (and therefore $\delta\Pi$) significantly. In future work, we shall attempt to find a relation between H_{ij} results for different shapes, so that H_{ij} could be calculated for a single shape and translated to other shapes by a simple connection, thus further decreasing the amount of H_{ij} calculations - to be performed only once - in order to find $\delta\Pi$ for all variables. We will also attempt to improve the existing dependence of H_{ij} on different values of ν so that it could be calculated for one reference material only.

The extension of the failure initiation criterion in [6] to V-notch edges necessitates an expression of $\delta\Pi$ as presented herein (vertex singularities are not addressed herein). This expression will be utilized in a future publication to predict crack initiation location and instance in 3D brittle elastic materials containing sharp V-notches under a complex stress state.

Acknowledgements

The authors thank Dr. Elad Priel and Prof. Jacob Bortman for many fruitful discussions. This research was supported by the Israel Science Foundation (grant No. 444/10).

Appendix A. Derivation of $\delta\Pi = \Psi\left[u^{near}, u^{far}\right] = -\frac{1}{2}\int\limits_{\Gamma^*_{sph}} \left(\mathcal{T}(u^{near})u^{far} - \mathcal{T}(u^{far})u^{near}\right) d\Gamma$

$\delta\Pi$ represents the difference in potential energy between two domains - with and without a crack. The presence of a crack is the only difference between the two, so that the rest of the geometry and boundary conditions are identical. We introduce notations for the displacement and stress fields: for a domain with a crack: $\sigma_{ij}^{(c)}$, $u_i^{(c)}$ and without a crack $\sigma_{ij}^{(nc)}$, $u_i^{(nc)}$. These represent the displacements and stresses throughout the entire domain (u^{far} and u^{near} represent the displacements well only in the vicinity of a V-notch tip, and in the vicinity of a crack initiating from a V-notch edge, respectively). Ω^D and $\partial\Omega^D$ are the domain without a crack and its surface, whereas Ω_c^D and $\partial\Omega_c^D$ are the domain containing a crack and its surface.

For Ω^D the potential energy is:

$$\Pi(u^{(nc)}) = \frac{1}{2}\int\limits_{\Omega^D} \sigma_{ij}^{(nc)} u_{i,j}^{(nc)} d\Omega - \int\limits_{\partial\Omega^D} \sigma_{ij}^{(nc)} n_j u_i^{(nc)} d\Gamma - \int\limits_{\Omega^D} f_i u_i^{(nc)} d\Omega \tag{A.1}$$

where f_i are components of body forces. For Ω_c^D the potential energy is:

$$\Pi(u^{(c)}) = \frac{1}{2}\int\limits_{\Omega_c^D} \sigma_{ij}^{(c)} u_{i,j}^{(c)} d\Omega - \int\limits_{\partial\Omega_c^D} \sigma_{ij}^{(c)} n_j u_i^{(c)} d\Gamma - \int\limits_{\Omega_c^D} f_i u_i^{(c)} d\Omega \tag{A.2}$$

The difference in potential energy is:

$$\begin{aligned}\delta\Pi &= \Pi(u^{(c)}) - \Pi(u^{(nc)}) \\ &= -\int\limits_{\partial\Omega_c^D} \sigma_{ij}^{(c)} n_j u_i^{(c)} d\Gamma + \int\limits_{\partial\Omega^D} \sigma_{ij}^{(nc)} n_j u_i^{(nc)} d\Gamma + \frac{1}{2}\int\limits_{\Omega_c^D} \sigma_{ij}^{(c)} u_{i,j}^{(c)} d\Omega - \int\limits_{\Omega_c^D} f_i u_i^{(c)} d\Omega - \frac{1}{2}\int\limits_{\Omega^D} \sigma_{ij}^{(nc)} u_{i,j}^{(nc)} d\Omega + \int\limits_{\Omega^D} f_i u_i^{(nc)} d\Omega\end{aligned} \tag{A.3}$$

Using Cauchy's law, $\mathcal{T}_i = \sigma_{ij} n_j$, assuming no body forces - $f_i = 0$, and using the product rule $\sigma_{ij} u_{i,j} = (\sigma_{ij} u_i)_{,j} - \sigma_{ij,j} u_i$ we obtain:

$$\delta\Pi = -\int\limits_{\partial\Omega_c^D} \mathcal{T}_i^{(c)} u_i^{(c)} d\Gamma + \int\limits_{\partial\Omega^D} \mathcal{T}_i^{(nc)} u_i^{(nc)} d\Gamma + \frac{1}{2}\int\limits_{\Omega_c^D} ((\sigma_{ij}^{(c)} u_i^{(c)})_{,j} - \sigma_{ij,j}^{(c)} u_i^{(c)}) d\Omega - \frac{1}{2}\int\limits_{\Omega^D} ((\sigma_{ij}^{(nc)} u_i^{(nc)})_{,j} - \sigma_{ij,j}^{(nc)} u_i^{(nc)}) d\Omega \tag{A.4}$$

The stress tensor satisfies the equilibrium equation $\sigma_{ij,j} = 0$, so (A.4) becomes:

$$\delta\Pi = -\int\limits_{\partial\Omega_c^D} \mathcal{T}_i^{(c)} u_i^{(c)} d\Gamma + \int\limits_{\partial\Omega^D} \mathcal{T}_i^{(nc)} u_i^{(nc)} d\Gamma + \frac{1}{2}\int\limits_{\Omega_c^D} (\sigma_{ij}^{(c)} u_i^{(c)})_{,j} d\Omega - \frac{1}{2}\int\limits_{\Omega^D} (\sigma_{ij}^{(nc)} u_i^{(nc)})_{,j} d\Omega \tag{A.5}$$

By the divergence theorem $\int\limits_{\Omega} \mathbf{F}_{,j} d\Omega = \int\limits_{\Gamma} (\mathbf{F}\cdot\mathbf{n})\, d\Gamma$ and we have:

$$\begin{aligned}\delta\Pi &= -\int\limits_{\partial\Omega_c^D} \mathcal{T}_i^{(c)} u_i^{(c)} d\Gamma + \int\limits_{\partial\Omega^D} \mathcal{T}_i^{(nc)} u_i^{(nc)} d\Gamma + \frac{1}{2}\int\limits_{\partial\Omega_c^D} \sigma_{ij}^{(c)} n_j u_i^{(c)} d\Gamma - \frac{1}{2}\int\limits_{\partial\Omega^D} \sigma_{ij}^{(nc)} n_j u_i^{(nc)} d\Gamma \\ &= -\int\limits_{\partial\Omega_c^D} \mathcal{T}_i^{(c)} u_i^{(c)} d\Gamma + \int\limits_{\partial\Omega^D} \mathcal{T}_i^{(nc)} u_i^{(nc)} d\Gamma + \frac{1}{2}\int\limits_{\partial\Omega_c^D} \mathcal{T}_i^{(c)} u_i^{(c)} d\Gamma - \frac{1}{2}\int\limits_{\partial\Omega^D} \mathcal{T}_i^{(nc)} u_i^{(nc)} d\Gamma \\ &= -\frac{1}{2}\int\limits_{\partial\Omega_c^D} \mathcal{T}_i^{(c)} u_i^{(c)} d\Gamma + \frac{1}{2}\int\limits_{\partial\Omega^D} \mathcal{T}_i^{(nc)} u_i^{(nc)} d\Gamma\end{aligned} \tag{A.6}$$

Same tractions are applied on both $\partial\Omega^D$ and $\partial\Omega_c^D$ and the crack is traction-free, so:

$$\mathcal{T}_i^{(nc)} = \mathcal{T}_i^{(c)} \tag{A.7}$$

Therefore we may interchange $\mathcal{T}_i^{(nc)}$ and $\mathcal{T}_i^{(c)}$ in (A.6):

$$\delta\Pi = -\tfrac{1}{2}\int\limits_{\partial\Omega_c^D} \mathcal{T}_i^{(nc)} u_i^{(c)} d\Gamma + \tfrac{1}{2}\int\limits_{\partial\Omega^D} \mathcal{T}_i^{(c)} u_i^{(nc)} d\Gamma \tag{A.8}$$

The crack surfaces are traction free, so in the first term in (A.8), $\partial\Omega_c^D$ can be changed to $\partial\Omega^D$. Thus (A.8) becomes:

$$\delta\Pi = -\frac{1}{2}\int\limits_{\partial\Omega^D} \mathcal{T}_i^{(nc)} u_i^{(c)} d\Gamma + \frac{1}{2}\int\limits_{\partial\Omega^D} \mathcal{T}_i^{(c)} u_i^{(nc)} d\Gamma = \frac{1}{2}\int\limits_{\partial\Omega^D} \left(\mathcal{T}_i^{(c)} u_i^{(nc)} - \mathcal{T}_i^{(nc)} u_i^{(c)}\right) d\Gamma \tag{A.9}$$

Let us apply (A.6) on a spherical domain in the vicinity of a crack. Denote by Ω_c^{sph} a small spherical region in V-notch vicinity (see Fig. A.15-A.16). The outer part of the domain $\Omega^D - \Omega^{sph} = \Omega_c^D - \Omega_c^{sph}$ is in green in Fig. A.15.

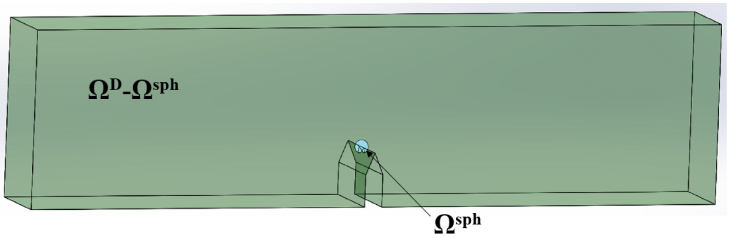

Figure A.15: Outer domain - schematic presentation

Throughout $\Omega^D - \Omega^{sph}$ and $\Omega_c^D - \Omega_c^{sph}$, the elastic solution is identical and independent of the presence of a crack, so that $\sigma_{ij}^{(c)} = \sigma_{ij}^{(nc)}$, $u_i^{(c)} = u_i^{(nc)}$. Therefore in the outer parts we obtain $\delta\Pi \equiv 0$, and $\delta\Pi$ is only because of Ω^{sph} and Ω_c^{sph}.

$\partial\Omega_c^{sph}$ is composed of the V-notch faces Γ_1, Γ_2, the crack faces Γ_3, Γ_4, and the spherical part of the surface Γ^{sph}, see Fig. A.16.

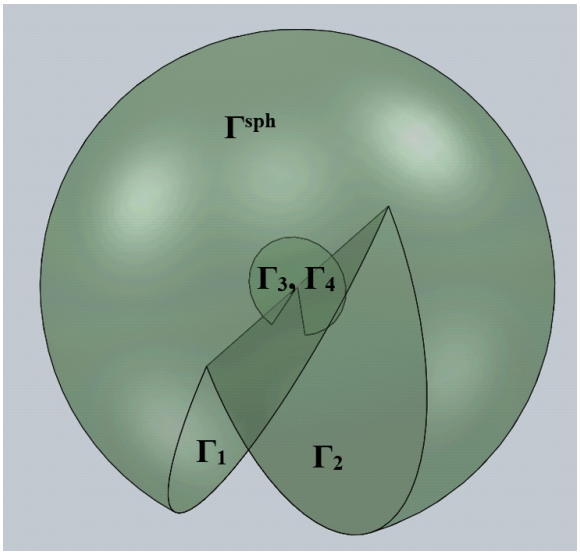

Figure A.16: The domain Ω_c^{sph}

In Ω_c^{sph} , $\sigma_{ij}^{(c)} = \sigma_{ij}^{near}$ and $u_i^{(c)} = u_i^{near}$, whereas in Ω^{sph} , $\sigma_{ij}^{(nc)} = \sigma_{ij}^{far}$ and $u_i^{(nc)} = u_i^{far}$. Over Γ^{sph} , $u_i^{far} = u_i^{near}$ (but $\mathcal{T}^{far} \neq \mathcal{T}^{near}$). Eq. (A.6) is then:

$$\delta\Pi = \Pi(u^{(c)}) - \Pi(u^{(nc)}) = \Pi(u^{near}) - \Pi(u^{far}) = -\frac{1}{2}\int\limits_{\partial\Omega_c} \mathcal{T}_i^{near} u_i^{near} d\Gamma + \frac{1}{2}\int\limits_{\partial\Omega} \mathcal{T}_i^{far} u_i^{far} d\Gamma \tag{A.10}$$

Since $\mathcal{T}_i^{near} = \mathcal{T}_i^{far} = 0$ on $\Gamma_1, \Gamma_2, \Gamma_3, \Gamma_4$ (A.10) becomes:

$$\delta\Pi = \frac{1}{2}\int\limits_{\Gamma_{sph}} \mathcal{T}_i^{far} u_i^{far} d\Gamma - \frac{1}{2}\int\limits_{\Gamma^{sph}} \mathcal{T}_i^{near} u_i^{near} d\Gamma \tag{A.11}$$

Since $u_i^{far} = u_i^{near}$ on Γ^{sph} :

$$\delta\Pi = \frac{1}{2}\int\limits_{\Gamma^{sph}} \left(\mathcal{T}_i^{far} u_i^{near} - \mathcal{T}_i^{near} u_i^{far}\right) d\Gamma \tag{A.12}$$

Which is (A.9), with an opposite sign.

Appendix B. Derivation of the explicit expression of $\delta\Pi$ in 3D domains

The derivation of the expression for $\delta\Pi$ (21) from (20) is detailed.
$\delta\Pi$ is a result of a crack of area S at the tip of the V-notched domain at $z = z_0$ as given in (A.12):

$$\delta\Pi = \Psi\left[\boldsymbol{u}^{near}, \boldsymbol{u}^{far}\right] \triangleq -\frac{1}{2}\int\limits_{\Gamma^{sph}} \left(\mathcal{T}(\boldsymbol{u}^{near})\boldsymbol{u}^{far} - \mathcal{T}(\boldsymbol{u}^{far})\boldsymbol{u}^{near}\right) d\Gamma \tag{B.1}$$

The integral is calculated over the spherical part of Ω_c^* . Inserting (9) and (13) in (B.1) and using the linearity property of the functional Ψ one obtains:

$$\begin{aligned}
\delta\Pi \quad = \quad & \Psi[\boldsymbol{u}^0(0,0,0), \boldsymbol{u}^0(0,0,0)] + \Psi[\boldsymbol{u}^0(0,0,0)\,,\, A_1 \times (\sqrt{S})^{\alpha_1} \times (\rho^* sin\varphi)^{\alpha_1} \times \boldsymbol{s}_{10}(\theta)] \\
& + \Psi[\boldsymbol{u}^0(0,0,0), A_2 \times (\sqrt{S})^{\alpha_2} \times (\rho^* sin\varphi)^{\alpha_2} \times \boldsymbol{s}_{20}(\theta)] + \Psi[\boldsymbol{u}^0(0,0,0), A_3 \times (\sqrt{S})^{\alpha_3} \times (\rho^* sin\varphi)^{\alpha_3} \times \boldsymbol{s}_{30}(\theta)] \\
& + \Psi[A_1 \times (\sqrt{S})^{\alpha_1} \times \left((\rho^* sin\varphi)^{\alpha_1} \times \boldsymbol{s}_{10}(\theta) + \hat{\mathbf{V}}_1(\rho^*, \varphi, \theta)\right), \boldsymbol{u}^0(0,0,0)] \\
& + \Psi[A_1 \times (\sqrt{S})^{\alpha_1} \times \left((\rho^* sin\varphi)^{\alpha_1} \times \boldsymbol{s}_{10}(\theta) + \hat{\mathbf{V}}_1(\rho^*, \varphi, \theta)\right)\,,\, A_1 \times (\sqrt{S})^{\alpha_1} \times (\rho^* sin\varphi)^{\alpha_1} \times \boldsymbol{s}_{10}(\theta)] \\
& + \Psi[A_1 \times (\sqrt{S})^{\alpha_1} \times \left((\rho^* sin\varphi)^{\alpha_1} \times \boldsymbol{s}_{10}(\theta) + \hat{\mathbf{V}}_1(\rho^*, \varphi, \theta)\right)\,,\, A_2 \times (\sqrt{S})^{\alpha_2} \times (\rho^* sin\varphi)^{\alpha_2} \times \boldsymbol{s}_{20}(\theta)] \\
& + \Psi[A_1 \times (\sqrt{S})^{\alpha_1} \times \left((\rho^* sin\varphi)^{\alpha_1} \times \boldsymbol{s}_{10}(\theta) + \hat{\mathbf{V}}_1(\rho^*, \varphi, \theta)\right)\,,\, A_3 \times (\sqrt{S})^{\alpha_3} \times (\rho^* sin\varphi)^{\alpha_3} \times \boldsymbol{s}_{30}(\theta)] \\
& + \Psi[A_2 \times (\sqrt{S})^{\alpha_2} \times \left((\rho^* sin\varphi)^{\alpha_2} \times \boldsymbol{s}_{20}(\theta) + \hat{\mathbf{V}}_2(\rho^*, \varphi, \theta)\right), \boldsymbol{u}^0(0,0,0)] \\
& + \Psi[A_2 \times (\sqrt{S})^{\alpha_2} \times \left((\rho^* sin\varphi)^{\alpha_2} \times \boldsymbol{s}_{20}(\theta) + \hat{\mathbf{V}}_2(\rho^*, \varphi, \theta)\right)\,,\, A_1 \times (\sqrt{S})^{\alpha_1} \times (\rho^* sin\varphi)^{\alpha_1} \times \boldsymbol{s}_{10}(\theta)] \\
& + \Psi[A_2 \times (\sqrt{S})^{\alpha_2} \times \left((\rho^* sin\varphi)^{\alpha_2} \times \boldsymbol{s}_{20}(\theta) + \hat{\mathbf{V}}_2(\rho^*, \varphi, \theta)\right)\,,\, A_2 \times (\sqrt{S})^{\alpha_2} \times (\rho^* sin\varphi)^{\alpha_2} \times \boldsymbol{s}_{20}(\theta)] \\
& + \Psi[A_2 \times (\sqrt{S})^{\alpha_2} \times \left((\rho^* sin\varphi)^{\alpha_2} \times \boldsymbol{s}_{20}(\theta) + \hat{\mathbf{V}}_2(\rho^*, \varphi, \theta)\right)\,,\, A_3 \times (\sqrt{S})^{\alpha_3} \times (\rho^* sin\varphi)^{\alpha_3} \times \boldsymbol{s}_{30}(\theta)] \\
& + \Psi[A_3 \times (\sqrt{S})^{\alpha_3} \times \left((\rho^* sin\varphi)^{\alpha_3} \times \boldsymbol{s}_{30}(\theta) + \hat{\mathbf{V}}_3(\rho^*, \varphi, \theta)\right)\,,\, \boldsymbol{u}^0(0,0,0)] \\
& + \Psi[A_3 \times (\sqrt{S})^{\alpha_3} \times (\rho^* sin\varphi)^{\alpha_3} \times \boldsymbol{s}_{30}(\theta) + \hat{\mathbf{V}}_3(\rho^*, \varphi, \theta)\,,\, A_1 \times (\sqrt{S})^{\alpha_1} \times (\rho^* sin\varphi)^{\alpha_1} \times \boldsymbol{s}_{10}(\theta)] \\
& + \Psi[A_3 \times (\sqrt{S})^{\alpha_3} \times (\rho^* sin\varphi)^{\alpha_3} \times \boldsymbol{s}_{30}(\theta) + \hat{\mathbf{V}}_3(\rho^*, \varphi, \theta)\,,\, A_2 \times (\sqrt{S})^{\alpha_2} \times (\rho^* sin\varphi)^{\alpha_2} \times \boldsymbol{s}_{20}(\theta)] \\
& + \Psi[A_3 \times (\sqrt{S})^{\alpha_3} \times (\rho^* sin\varphi)^{\alpha_3} \times \boldsymbol{s}_{30}(\theta) + \hat{\mathbf{V}}_3(\rho^*, \varphi, \theta)\,,\, A_3 \times (\sqrt{S})^{\alpha_3} \times (\rho^* sin\varphi)^{\alpha_3} \times \boldsymbol{s}_{30}(\theta)] + \text{(H.O.T)}
\end{aligned} \tag{B.2}$$

For brevity, we denote:

$$\mathbf{D}_i(\rho^*, \varphi, \theta) = (\rho^* sin\varphi)^{\alpha_i} \boldsymbol{s}_{i0}(\theta) \tag{B.3}$$

i.e. (B.2) is:

$$
\begin{aligned}
\delta\Pi \;=\;& \Psi[\boldsymbol{u}^0(0,0,0),\boldsymbol{u}^0(0,0,0)] + \Psi[\boldsymbol{u}^0(0,0,0), A_1\times(\sqrt{S})^{\alpha_1}\times\mathbf{D}_1(\rho^*,\varphi,\theta)] \\
&+\Psi[\boldsymbol{u}^0(0,0,0), A_2\times(\sqrt{S})^{\alpha_2}\times\mathbf{D}_2(\rho^*,\varphi,\theta)] + \Psi[\boldsymbol{u}^0(0,0,0), A_3\times(\sqrt{S})^{\alpha_3}\times\mathbf{D}_3(\rho^*,\varphi,\theta)] \\
&+\Psi[A_1\times(\sqrt{S})^{\alpha_1}\times(\mathbf{D}_1(\rho^*,\varphi,\theta)+\hat{\mathbf{V}}_1(\rho^*,\varphi,\theta)),\ \boldsymbol{u}^0(0,0,0)] \\
&+\Psi[A_1\times(\sqrt{S})^{\alpha_1}\times(\mathbf{D}_1(\rho^*,\varphi,\theta)+\hat{\mathbf{V}}_1(\rho^*,\varphi,\theta)),\ A_1\times(\sqrt{S})^{\alpha_1}\times\mathbf{D}_1(\rho^*,\varphi,\theta)] \\
&+\Psi[A_1\times(\sqrt{S})^{\alpha_1}\times(\mathbf{D}_1(\rho^*,\varphi,\theta)+\hat{\mathbf{V}}_1(\rho^*,\varphi,\theta)),\ A_2\times(\sqrt{S})^{\alpha_2}\times\mathbf{D}_2(\rho^*,\varphi,\theta)] \\
&+\Psi[A_1\times(\sqrt{S})^{\alpha_1}\times(\mathbf{D}_1(\rho^*,\varphi,\theta)+\hat{\mathbf{V}}_1(\rho^*,\varphi,\theta)),\ A_3\times(\sqrt{S})^{\alpha_3}\times\mathbf{D}_3(\rho^*,\varphi,\theta)] \\
&+\Psi[A_2\times(\sqrt{S})^{\alpha_2}\times(\mathbf{D}_2(\rho^*,\varphi,\theta)+\hat{\mathbf{V}}_2(\rho^*,\varphi,\theta)),\ \boldsymbol{u}^0(0,0,0)] \\
&+\Psi[A_2\times(\sqrt{S})^{\alpha_2}\times(\mathbf{D}_2(\rho^*,\varphi,\theta)+\hat{\mathbf{V}}_2(\rho^*,\varphi,\theta)),\ A_1\times(\sqrt{S})^{\alpha_1}\times\mathbf{D}_1(\rho^*,\varphi,\theta)] \\
&+\Psi[A_2\times(\sqrt{S})^{\alpha_2}\times(\mathbf{D}_2(\rho^*,\varphi,\theta)+\hat{\mathbf{V}}_2(\rho^*,\varphi,\theta)),\ A_2\times(\sqrt{S})^{\alpha_2}\times\mathbf{D}_2(\rho^*,\varphi,\theta)] \\
&+\Psi[A_2\times(\sqrt{S})^{\alpha_2}\times(\mathbf{D}_2(\rho^*,\varphi,\theta)+\hat{\mathbf{V}}_2(\rho^*,\varphi,\theta)),\ A_3\times(\sqrt{S})^{\alpha_3}\times\mathbf{D}_3(\rho^*,\varphi,\theta)] \\
&+\Psi[A_3\times(\sqrt{S})^{\alpha_3}\times(\mathbf{D}_3(\rho^*,\varphi,\theta)+\hat{\mathbf{V}}_3(\rho^*,\varphi,\theta)),\ \boldsymbol{u}^0(0,0,0)] \\
&+\Psi[A_3\times(\sqrt{S})^{\alpha_3}\times(\mathbf{D}_3(\rho^*,\varphi,\theta)+\hat{\mathbf{V}}_3(\rho^*,\varphi,\theta)),\ A_1\times(\sqrt{S})^{\alpha_1}\times\mathbf{D}_1(\rho^*,\varphi,\theta)] \\
&+\Psi[A_3\times(\sqrt{S})^{\alpha_3}\times(\mathbf{D}_3(\rho^*,\varphi,\theta)+\hat{\mathbf{V}}_3(\rho^*,\varphi,\theta)),\ A_2\times(\sqrt{S})^{\alpha_2}\times\mathbf{D}_2(\rho^*,\varphi,\theta)] \\
&+\Psi[A_3\times(\sqrt{S})^{\alpha_3}\times(\mathbf{D}_3(\rho^*,\varphi,\theta)+\hat{\mathbf{V}}_3(\rho^*,\varphi,\theta)),\ A_3\times(\sqrt{S})^{\alpha_3}\times\mathbf{D}_3(\rho^*,\varphi,\theta)] + H.O.T. \qquad \text{(B.4)}
\end{aligned}
$$

By definition, $\Psi(\boldsymbol{g},\boldsymbol{g})\equiv 0$. In the 3D case, as opposed to the 2D case, *the eigenfunctions* $\boldsymbol{s}_{ij}(\theta)$ *are not bi-orthogonal for any chosen plane crack.*

$$
\begin{aligned}
\delta\Pi \;=\;& \Psi[\boldsymbol{u}^0(0,0,0), A_1\times(\sqrt{S})^{\alpha_1}\times\mathbf{D}_1(\rho^*,\varphi,\theta)] \\
&+\Psi[\boldsymbol{u}^0(0,0,0), A_2\times(\sqrt{S})^{\alpha_2}\times\mathbf{D}_2(\rho^*,\varphi,\theta)] + \Psi[\boldsymbol{u}^0(0,0,0), A_3\times(\sqrt{S})^{\alpha_3}\times\mathbf{D}_3(\rho^*,\varphi,\theta)] \\
&+\Psi[A_1\times(\sqrt{S})^{\alpha_1}\times(\mathbf{D}_1(\rho^*,\varphi,\theta)+\hat{\mathbf{V}}_1(\rho^*,\varphi,\theta)),\boldsymbol{u}^0(0,0,0)] \\
&+\Psi[A_1\times(\sqrt{S})^{\alpha_1}\times\hat{\mathbf{V}}_1(\rho^*,\varphi,\theta), A_1\times(\sqrt{S})^{\alpha_1}\times\mathbf{D}_1(\rho^*,\varphi,\theta)] \\
&+\Psi[A_1\times(\sqrt{S})^{\alpha_1}\times(\mathbf{D}_1(\rho^*,\varphi,\theta)+\hat{\mathbf{V}}_1(\rho^*,\varphi,\theta)), A_2\times(\sqrt{S})^{\alpha_2}\times\mathbf{D}_2(\rho^*,\varphi,\theta)] \\
&+\Psi[A_1\times(\sqrt{S})^{\alpha_1}\times(\mathbf{D}_1(\rho^*,\varphi,\theta)+\hat{\mathbf{V}}_1(\rho^*,\varphi,\theta)), A_3\times(\sqrt{S})^{\alpha_3}\times\mathbf{D}_3(\rho^*,\varphi,\theta)] \\
&+\Psi[A_2\times(\sqrt{S})^{\alpha_2}\times(\mathbf{D}_2(\rho^*,\varphi,\theta)+\hat{\mathbf{V}}_2(\rho^*,\varphi,\theta)),\boldsymbol{u}^0(0,0,0)] \\
&+\Psi[A_2\times(\sqrt{S})^{\alpha_2}\times(\mathbf{D}_2(\rho^*,\varphi,\theta)+\hat{\mathbf{V}}_2(\rho^*,\varphi,\theta)), A_1\times(\sqrt{S})^{\alpha_1}\times\mathbf{D}_1(\rho^*,\varphi,\theta)] \\
&+\Psi[A_2\times(\sqrt{S})^{\alpha_2}\times\hat{\mathbf{V}}_2(\rho^*,\varphi,\theta), A_2\times(\sqrt{S})^{\alpha_2}\times\mathbf{D}_2(\rho^*,\varphi,\theta)] \\
&+\Psi[A_2\times(\sqrt{S})^{\alpha_2}\times(\mathbf{D}_2(\rho^*,\varphi,\theta)+\hat{\mathbf{V}}_2(\rho^*,\varphi,\theta)), A_3\times(\sqrt{S})^{\alpha_3}\times\mathbf{D}_3(\rho^*,\varphi,\theta)] \\
&+\Psi[A_3\times(\sqrt{S})^{\alpha_3}\times(\mathbf{D}_3(\rho^*,\varphi,\theta)+\hat{\mathbf{V}}_3(\rho^*,\varphi,\theta)),\boldsymbol{u}^0(0,0,0)] \\
&+\Psi[A_3\times(\sqrt{S})^{\alpha_3}\times(\mathbf{D}_3(\rho^*,\varphi,\theta)+\hat{\mathbf{V}}_3(\rho^*,\varphi,\theta)), A_1\times(\sqrt{S})^{\alpha_1}\times\mathbf{D}_1(\rho^*,\varphi,\theta)] \\
&+\Psi[A_3\times(\sqrt{S})^{\alpha_3}\times(\mathbf{D}_3(\rho^*,\varphi,\theta)+\hat{\mathbf{V}}_3(\rho^*,\varphi,\theta)), A_2\times(\sqrt{S})^{\alpha_2}\times\mathbf{D}_2(\rho^*,\varphi,\theta)] \\
&+\Psi[A_3\times(\sqrt{S})^{\alpha_3}\times\hat{\mathbf{V}}_3(\rho^*,\varphi,\theta), A_3\times(\sqrt{S})^{\alpha_3}\times\mathbf{D}_3(\rho^*,\varphi,\theta)] + H.O.T. \qquad \text{(B.5)}
\end{aligned}
$$

$\boldsymbol{u}^0(0,0,0)$ is a constant vector, therefore $\mathcal{T}(\boldsymbol{u}^0(0,0,0))=0$ and the first three terms in (B.5) are:

$$
\begin{aligned}
&\Psi[\boldsymbol{u}^0(0,0,0)\,,\, A_i\times(\sqrt{S})^{\alpha_i}\times(\mathbf{D}_i(\rho^*,\varphi,\theta)+\hat{\mathbf{V}}_i(\rho^*,\varphi,\theta))] \\
&=-\tfrac{1}{2}[\int_{\Gamma}(\mathcal{T}(\boldsymbol{u}^0(0,0,0))\,A_i\times(\sqrt{S})^{\alpha_i}\times(\mathbf{D}_i(\rho^*,\varphi,\theta)+\hat{\mathbf{V}}_i(\rho^*,\varphi,\theta)) \\
&\quad -\mathcal{T}(A_i\times(\sqrt{S})^{\alpha_i}\times(\mathbf{D}_i(\rho^*,\varphi,\theta)+\hat{\mathbf{V}}_i(\rho^*,\varphi,\theta)))\times\boldsymbol{u}^0(0,0,0))]\,d\Gamma \\
&=\tfrac{\boldsymbol{u}^0(0,0,0)}{2}\int_{\Gamma}\mathcal{T}(A_i\times(\sqrt{S})^{\alpha_i}\times(\mathbf{D}_i(\rho^*,\varphi,\theta)+\hat{\mathbf{V}}_i(\rho^*,\varphi,\theta)))d\Gamma
\end{aligned}
$$

According to Gauss' theorem:

$$
\int\!\!\int_{V}\!\!\int(\nabla\cdot\boldsymbol{u})dV=\oiint_{\Gamma}\boldsymbol{u}\cdot d\boldsymbol{\Gamma} \qquad \text{(B.6)}
$$

where the right hand side is the surface integral over the boundary of the volume V (denoted here by Γ), and $d\boldsymbol{\Gamma}=\hat{\boldsymbol{n}}\cdot d\Gamma$ where $\hat{\boldsymbol{n}}$ is the outward unit normal vector of the boundary Γ. Using (B.6) the area integral can be transformed into a volume integral in which the elasticity operator acts on the eigenpair, obtaining:

$$\begin{aligned}
&\tfrac{\boldsymbol{u}^0(0,0,0)}{2}\int\limits_{\Gamma}\mathcal{T}\left\{A_i\times(\sqrt{S})^{\alpha_i}\times[\mathbf{D}_i(\rho^*,\varphi,\theta)+\hat{\mathbf{V}}_i(\rho^*,\varphi,\theta)]\right\}d\Gamma\\
&=\tfrac{\boldsymbol{u}^0(0,0,0)}{2}\int\limits_{V}\mathcal{L}\left\{A_i\times(\sqrt{S})^{\alpha_i}\times[\mathbf{D}_i(\rho^*,\varphi,\theta)+\hat{\mathbf{V}}_i(\rho^*,\varphi,\theta)]\right\}dV=0\,,
\end{aligned}\tag{B.7}$$

because $\mathcal{L}\{\ \}=0$. Thus $\Psi\left[\boldsymbol{u}^0(0,0,0),A_i\times(\sqrt{S})^{\alpha_i}\times[\mathbf{D}_i(\rho^*,\varphi,\theta)+\hat{\mathbf{V}}_i(\rho^*,\varphi,\theta)]\right]=0$, and (B.5) is simplified to:

$$\begin{aligned}
\delta\Pi \;=\;& \Psi[A_1\times(\sqrt{S})^{\alpha_1}\times\hat{\mathbf{V}}_1(\rho^*,\varphi,\theta),A_1\times(\sqrt{S})^{\alpha_1}\times\mathbf{D}_1(\rho^*,\varphi,\theta)]\\
&+\Psi[A_1\times(\sqrt{S})^{\alpha_1}\times\mathbf{D}_1(\rho^*,\varphi,\theta),A_2\times(\sqrt{S})^{\alpha_2}\times\mathbf{D}_2(\rho^*,\varphi,\theta)]\\
&+\Psi[A_1\times(\sqrt{S})^{\alpha_1}\times\hat{\mathbf{V}}_1(\rho^*,\varphi,\theta),A_2\times(\sqrt{S})^{\alpha_2}\times\mathbf{D}_2(\rho^*,\varphi,\theta)]\\
&+\Psi[A_1\times(\sqrt{S})^{\alpha_1}\times\mathbf{D}_1(\rho^*,\varphi,\theta),A_3\times(\sqrt{S})^{\alpha_3}\times\mathbf{D}_3(\rho^*,\varphi,\theta)]\\
&+\Psi[A_1\times(\sqrt{S})^{\alpha_1}\times\hat{\mathbf{V}}_1(\rho^*,\varphi,\theta),A_3\times(\sqrt{S})^{\alpha_3}\times\mathbf{D}_3(\rho^*,\varphi,\theta)]\\
&+\Psi[A_2\times(\sqrt{S})^{\alpha_2}\times\mathbf{D}_2(\rho^*,\varphi,\theta),A_1\times(\sqrt{S})^{\alpha_1}\times\mathbf{D}_1(\rho^*,\varphi,\theta)]\\
&+\Psi[A_2\times(\sqrt{S})^{\alpha_2}\times\hat{\mathbf{V}}_2(\rho^*,\varphi,\theta),A_1\times(\sqrt{S})^{\alpha_1}\times\mathbf{D}_1(\rho^*,\varphi,\theta)]\\
&+\Psi[A_2\times(\sqrt{S})^{\alpha_2}\times\hat{\mathbf{V}}_2(\rho^*,\varphi,\theta),A_2\times(\sqrt{S})^{\alpha_2}\times\mathbf{D}_2(\rho^*,\varphi,\theta)]\\
&+\Psi[A_2\times(\sqrt{S})^{\alpha_2}\times\mathbf{D}_2(\rho^*,\varphi,\theta),A_3\times(\sqrt{S})^{\alpha_3}\times\mathbf{D}_3(\rho^*,\varphi,\theta)]\\
&+\Psi[A_2\times(\sqrt{S})^{\alpha_2}\times\hat{\mathbf{V}}_2(\rho^*,\varphi,\theta),A_3\times(\sqrt{S})^{\alpha_3}\times\mathbf{D}_3(\rho^*,\varphi,\theta)]\\
&+\Psi[A_3\times(\sqrt{S})^{\alpha_3}\times\mathbf{D}_3(\rho^*,\varphi,\theta),A_1\times(\sqrt{S})^{\alpha_1}\times\mathbf{D}_1(\rho^*,\varphi,\theta)]\\
&+\Psi[A_3\times(\sqrt{S})^{\alpha_3}\times\hat{\mathbf{V}}_3(\rho^*,\varphi,\theta),A_1\times(\sqrt{S})^{\alpha_1}\times\mathbf{D}_1(\rho^*,\varphi,\theta)]\\
&+\Psi[A_3\times(\sqrt{S})^{\alpha_3}\times\mathbf{D}_3(\rho^*,\varphi,\theta),A_2\times(\sqrt{S})^{\alpha_2}\times\mathbf{D}_2(\rho^*,\varphi,\theta)]\\
&+\Psi[A_3\times(\sqrt{S})^{\alpha_3}\times\hat{\mathbf{V}}_3(\rho^*,\varphi,\theta),A_2\times(\sqrt{S})^{\alpha_2}\times\mathbf{D}_2(\rho^*,\varphi,\theta)]\\
&+\Psi[A_3\times(\sqrt{S})^{\alpha_3}\times\hat{\mathbf{V}}_3(\rho^*,\varphi,\theta),A_3\times(\sqrt{S})^{\alpha_3}\times\mathbf{D}_3(\rho^*,\varphi,\theta)]+H.O.T.\\
\\
=\;& A_1^2\times(\sqrt{S})^{2\alpha_1}\times\Psi[\hat{\mathbf{V}}_1(\rho^*,\varphi,\theta),\mathbf{D}_1(\rho^*,\varphi,\theta)]\\
&+A_1\,A_2\times(\sqrt{S})^{\alpha_1+\alpha_2}\times\Psi[\mathbf{D}_1(\rho^*,\varphi,\theta),\mathbf{D}_2(\rho^*,\varphi,\theta)]\\
&+A_1\,A_2\times(\sqrt{S})^{\alpha_1+\alpha_2}\times\Psi[\hat{\mathbf{V}}_1(\rho^*,\varphi,\theta),\mathbf{D}_2(\rho^*,\varphi,\theta)]\\
&+A_1\,A_3\times(\sqrt{S})^{\alpha_1+\alpha_3}\times\Psi[\mathbf{D}_1(\rho^*,\varphi,\theta),\mathbf{D}_3(\rho^*,\varphi,\theta)]\\
&+A_1\,A_3\times(\sqrt{S})^{\alpha_1+\alpha_3}\times\Psi[\hat{\mathbf{V}}_1(\rho^*,\varphi,\theta),\mathbf{D}_3(\rho^*,\varphi,\theta)]\\
&+A_1\,A_2\times(\sqrt{S})^{\alpha_1+\alpha_2}\times\Psi[\mathbf{D}_2(\rho^*,\varphi,\theta),\mathbf{D}_1(\rho^*,\varphi,\theta)]\\
&+A_1\,A_2\times(\sqrt{S})^{\alpha_1+\alpha_2}\times\Psi[\hat{\mathbf{V}}_2(\rho^*,\varphi,\theta),\mathbf{D}_1(\rho^*,\varphi,\theta)]\\
&+A_2^2\times(\sqrt{S})^{2\alpha_2}\times\Psi[\hat{\mathbf{V}}_2(\rho^*,\varphi,\theta),\mathbf{D}_2(\rho^*,\varphi,\theta)]\\
&+A_2\,A_3\times(\sqrt{S}))^{\alpha_2+\alpha_3}\times\Psi[\mathbf{D}_2(\rho^*,\varphi,\theta),\mathbf{D}_3(\rho^*,\varphi,\theta)]\\
&+A_2\,A_3\times(\sqrt{S}))^{\alpha_2+\alpha_3}\times\Psi[\hat{\mathbf{V}}_2(\rho^*,\varphi,\theta),\mathbf{D}_3(\rho^*,\varphi,\theta)]\\
&+A_1\,A_3\times(\sqrt{S})^{\alpha_1+\alpha_3}\times\Psi[\mathbf{D}_3(\rho^*,\varphi,\theta),\mathbf{D}_1(\rho^*,\varphi,\theta)]\\
&+A_1\,A_3\times(\sqrt{S})^{\alpha_1+\alpha_3}\times\Psi[\hat{\mathbf{V}}_3(\rho^*,\varphi,\theta),\mathbf{D}_1(\rho^*,\varphi,\theta)]\\
&+A_2\,A_3\times(\sqrt{S}))^{\alpha_2+\alpha_3}\times\Psi[\mathbf{D}_3(\rho^*,\varphi,\theta),\mathbf{D}_2(\rho^*,\varphi,\theta)]\\
&+A_2\,A_3\times(\sqrt{S}))^{\alpha_2+\alpha_3}\times\Psi[\hat{\mathbf{V}}_3(\rho^*,\varphi,\theta),\mathbf{D}_2(\rho^*,\varphi,\theta)]\\
&+A_3^2\times(\sqrt{S})^{2\alpha_3}\times\Psi[\hat{\mathbf{V}}_3(\rho^*,\varphi,\theta),\mathbf{D}_3(\rho^*,\varphi,\theta)]+H.O.T.
\end{aligned}\tag{B.8}$$

We define I_{ij} :

$$I_{ij}\triangleq-\Psi\left[\mathbf{D}_i(\rho^*,\varphi,\theta),\mathbf{D}_j(\rho^*,\varphi,\theta)\right]=-\Psi\left[(\rho^*\,sin\varphi)^{\alpha_i}\times\boldsymbol{s}_{i0}(\theta),(\rho^*\,sin\varphi)^{\alpha_j}\times\boldsymbol{s}_{j0}(\theta)\right]\tag{B.9}$$

where $\boldsymbol{s}_{i\,0}(\theta)$ are given in (5).

I_{ij} in the $\delta\Pi$ expressions (eq. B.8) appears in pairs: $I_{ij}+I_{ji}$ for $i\neq j$. By definition, $I_{ij}+I_{ji}=0$ since $I_{ij}+I_{ji}=\frac{1}{2}\int\limits_{\Gamma}\left(\mathcal{T}(\mathbf{D}_i)\mathbf{D}_j-\mathcal{T}(\mathbf{D}_j)\mathbf{D}_i\right)d\Gamma+\frac{1}{2}\int\limits_{\Gamma}\left(\mathcal{T}(\mathbf{D}_j)\mathbf{D}_i-\mathcal{T}(\mathbf{D}_i)\mathbf{D}_j\right)d\Gamma\equiv0$.

Therefore (B.8) simplifies to:

$$\begin{aligned}\delta\Pi &= A_1^2 \times (\sqrt{S})^{2\alpha_1} \times \Psi[\hat{\mathbf{V}}_1(\rho^*,\varphi,\theta), \mathbf{D}_1(\rho^*,\varphi,\theta)] \\ &\quad + A_1\, A_2 \times (\sqrt{S})^{\alpha_{1+}\alpha_2} \times \Psi[\hat{\mathbf{V}}_1(\rho^*,\varphi,\theta), \mathbf{D}_2(\rho^*,\varphi,\theta)] \\ &\quad + A_1\, A_3 \times (\sqrt{S})^{\alpha_1+\alpha_3} \times \Psi[\hat{\mathbf{V}}_1(\rho^*,\varphi,\theta), \mathbf{D}_3(\rho^*,\varphi,\theta)] \\ &\quad + A_1\, A_2 \times (\sqrt{S})^{\alpha_{1+}\alpha_2} \times \Psi[\hat{\mathbf{V}}_2(\rho^*,\varphi,\theta), \mathbf{D}_1(\rho^*,\varphi,\theta)] \\ &\quad + A_2^2 \times (\sqrt{S})^{2\alpha_2} \times \Psi[\hat{\mathbf{V}}_2(\rho^*,\varphi,\theta), \mathbf{D}_2(\rho^*,\varphi,\theta)] \\ &\quad + A_2\, A_3 \times (\sqrt{S}))^{\alpha_{2+}\alpha_3} \times \Psi[\hat{\mathbf{V}}_2(\rho^*,\varphi,\theta), \mathbf{D}_3(\rho^*,\varphi,\theta)] \\ &\quad + A_1\, A_3 \times (\sqrt{S})^{\alpha_{1+}\alpha_3} \times \Psi[\hat{\mathbf{V}}_3(\rho^*,\varphi,\theta), \mathbf{D}_1(\rho^*,\varphi,\theta)] \\ &\quad + A_2\, A_3 \times (\sqrt{S}))^{\alpha_{2+}\alpha_3} \times \Psi[\hat{\mathbf{V}}_3(\rho^*,\varphi,\theta), \mathbf{D}_2(\rho^*,\varphi,\theta)] \\ &\quad + A_3^2 \times (\sqrt{S})^{2\alpha_3} \times \Psi[\hat{\mathbf{V}}_3(\rho^*,\varphi,\theta), \mathbf{D}_3(\rho^*,\varphi,\theta)] + H.O.T. \end{aligned} \tag{B.10}$$

or in general:

$$\delta\Pi = \sum_{i=1}^{3}\sum_{j=1}^{3} A_i\, A_j \times (\sqrt{S})^{\alpha_i+\alpha_j} \times \Psi[\hat{\mathbf{V}}_i, \mathbf{D}_j] + H.O.T. \tag{B.11}$$

Substituting (B.3) into (B.11) one obtains:

$$\delta\Pi = \sum_{i=1}^{3}\sum_{j=1}^{3} A_i\, A_j \times (\sqrt{S})^{\alpha_i+\alpha_j} \times \Psi[\hat{\mathbf{V}}_i\,,\, (\rho^* \times sin\varphi)^{\alpha_j} \times \boldsymbol{s}_{j0}(\theta)] + H.O.T. \tag{B.12}$$

Using the definition of H_{ij} in (26) we finally have:

$$-\delta\Pi = \sum_{i=1}^{3}\sum_{j=1}^{3} A_i\, A_j \times (\sqrt{S})^{\alpha_i+\alpha_j+1}\, H_{ij} \tag{B.13}$$

Appendix C. Computing H_{ii} by an alternative method

We have found an alternative method for calculating H_{ii} functions. This method uses the observation that the potential energy of the spherical domain itself (denoted by $\Pi^{\Omega_c^{*sph}}$) is actually $\delta\Pi$, for a special case of a unit area crack and unit GESIFs $A_i(z)$, which is by (28):

$$\Pi^{\Omega_c^{*sph}} = \delta\Pi = -\sum_{i,j} H_{ij} \tag{C.1}$$

We have shown in Appendix A that $\delta\Pi$ is confined to the spherical volumes with and without a crack Ω^{sph} and Ω_c^{sph}, so $\delta\Pi = \Pi^{\Omega_c^{sph}} - \Pi^{\Omega^{sph}}$. The displacements solution is u^{far} (9) within Ω^{sph}, and u^{near} (13) within Ω_c^{sph}. From matching the far and near fields as $\rho^* \to \infty$ we have obtained a representation of u^{near} as:

$$\begin{aligned}\boldsymbol{u}^{near}(\rho^*\sqrt{S},\varphi,\theta) &= \boldsymbol{u}^0(0,0,0) + A_1 \times (\sqrt{S})^{\alpha_1} \times [(\rho^* \times sin\varphi)^{\alpha_1} \times \boldsymbol{s}_{10}(\theta) + \hat{\mathbf{V}}_1(\rho^*,\varphi,\theta)] \\ &\quad + A_2 \times (\sqrt{S})^{\alpha_2} \times [(\rho^* \times sin\varphi)^{\alpha_2} \times \boldsymbol{s}_{20}(\theta) + \hat{\mathbf{V}}_2(\rho^*,\varphi,\theta)] \\ &\quad + A_3 \times (\sqrt{S})^{\alpha_3} \times [(\rho^* \times sin\varphi)^{\alpha_3} \times \boldsymbol{s}_{30}(\theta) + \hat{\mathbf{V}}_3(\rho^*,\varphi,\theta)] + ... \\ &= \boldsymbol{u}^{far}(\rho^*\sqrt{S},\varphi,\theta) + \sum_{i=1}^{3} A_i \times (\sqrt{S})^{\alpha_i}\, \hat{\mathbf{V}}_i(\rho^*,\varphi,\theta) \end{aligned} \tag{C.2}$$

so that:

$$\delta\Pi = \Pi^{\Omega_c^{sph}} - \Pi^{\Omega^{sph}} = \Pi\left(\boldsymbol{u}^{far} + \sum_{i=1}^{3} A_i \times (\sqrt{S})^{\alpha_i}\,\hat{\mathbf{V}}_i\right) - \Pi\left(\boldsymbol{u}^{far}\right) = \Pi\left(\sum_{i=1}^{3} A_i \times (\sqrt{S})^{\alpha_i}\,\hat{\mathbf{V}}_i\right) \qquad \text{(C.3)}$$

Eq. (C.3) can be regarded as superposition. Since outside Ω^{sph} and Ω_c^{sph}, the displacements, strains and stresses are identical $(\hat{\mathbf{V}}_i \sim 0)$ then also $\delta\Pi = \Pi^{\Omega_c^D} - \Pi^{\Omega^D}$. This is illustrated in Fig. C.17.

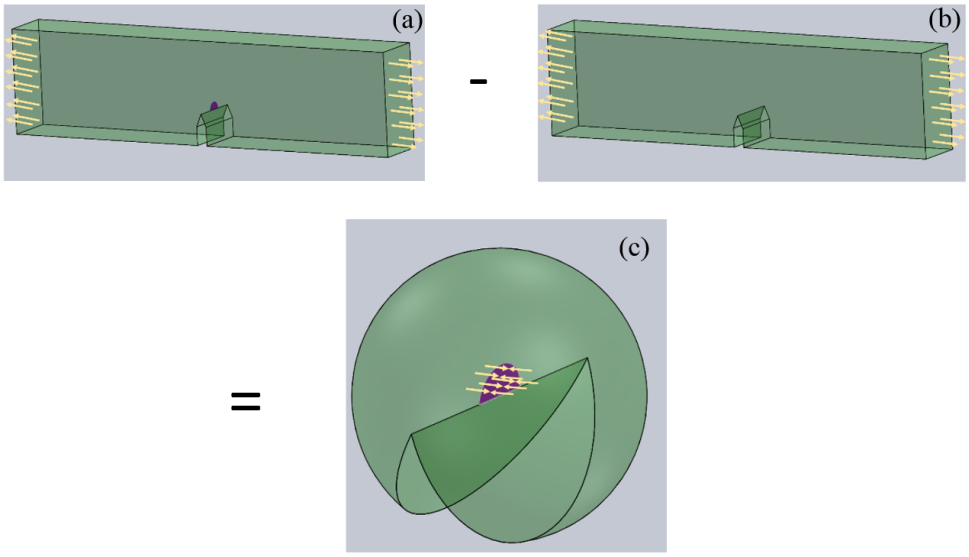

Figure C.17: Illustration of the superposition principle. (a) The bar-shaped model with a V-notch and a crack, (b) same model without a crack, and (c) the spherical domain with BCs on its faces that "elliminate" its presence.

In subsections 3.1- 3.2 we have shown that the spherical model represents the $\hat{\mathbf{V}}_i$ solution domain (Ω_c^{*sph}). The $\hat{\mathbf{V}}_i$ solution is defined for unit GESIFs $A_i(z)$ and in "stretched" coordinates, so the crack has unit area $(S^* = 1)$, and the spherical model was constructed accordingly. Using (28) and (C.3) we obtain (C.1).

The boundary conditions of the Ω_c^{*sph} domain are obtained from the asymptotic expasion, eq. (14)-(16). The V-notch faces remain traction-free. The tractions on the crack faces are minus those present on the chosen plane for a V-notch without a crack (16), and can be therefore regarded as "compensating" for its presence. The outer surface of the spherical domain is clamped (since $\hat{\mathbf{V}}_i \underset{\rho^* \to \infty}{\sim} 0$), this was not shown in Fig. C.17 (c).

If one applies modes 1,2 and 3 boundary conditions separately on the crack surfaces, then by (C.1) one obtains $|\Pi^{\Omega_c^{*sph}}| = |H_{11}|$ for mode 1 boundary conditions, $|\Pi^{\Omega_c^{*sph}}| = |H_{22}|$ for mode 2, and $|\Pi^{\Omega_c^{*sph}}| = |H_{33}|$ for mode 3. The potential energy of the FE model $\Pi^{\Omega_c^{*sph}}$ is computed by the FE analysis. This way we may compute H_{ii} for $i = 1, 2 \text{ or } 3$ by an alternative method and compare to the results computed by (30). The comparison was performed both for 2D cases [6] - in Table C.6, and for 3D cases - in Tables C.7, C.8 and C.9. The results obtained by the described method are denoted by H_{ii}^{2D} in 2D, and the crack angle θ was measured from the x axis. The parameters are: a V-notch angle $\omega = 315^o$, outer domain radius of $R = 200$, material properties of PMMA ($E = 3900\,MPa$, $\nu = 0.332$), polynomial degree of $p = 8$ and 90 Gauss integration points. The relative difference between the values obtained by both methods is also presented in the tables. In 3D the results obtained by the aforementioned method are denoted by $H_{ii}^{\Omega^*}$, and the results obtained by (30) are denoted by H_{ii}. The numerical results presented in Table C.7 and C.8 were for V-notch solid angle of 315^o, outer domain radius of $R = 100$, material properties of PMMA, polynomial degree of $p = 6$ and 54 Gauss points (the difference in H_{ii} compared with $p = 7$ and 90 Gauss points was less than 1% and is significantly more computationally expensive). The results presented in Table C.7 are for half a circle crack and crack orientation of (100), (-110), $(-\sqrt{3}10)$.

Simplified illustrations of models with the examined orientations are presented in Fig. 7, see also Fig. 8. The results presented in Table C.8 are for circular cracks orientations in (-101), (111), (212) and $(51(-3))$ (see Fig. 9). The results presented in Table C.9 are for half an ellipse crack with orientations (100), (-110), $(-\sqrt{3}10)$. The major (longer) axis of the ellipse a coincides with the V-notch edge (z axis) and is twice longer than the minor axis b ($a/b = 2$, see Fig. 13).

loading conditions on crack surface	mode I			mode II		
calculation method / crack angle θ	H_{11}	H_{11}^{2D}	% difference	H_{22}	H_{22}^{2D}	% difference
155	$1.28 \cdot 10^{-3}$	$1.268 \cdot 10^{-3}$	1	$9.421 \cdot 10^{-4}$	$9.339 \cdot 10^{-4}$	0.87
160	$1.324 \cdot 10^{-3}$	$1.311 \cdot 10^{-3}$	1	$9.035 \cdot 10^{-4}$	$8.957 \cdot 10^{-4}$	0.87
165	$1.358 \cdot 10^{-3}$	$1.345 \cdot 10^{-3}$	1	$8.715 \cdot 10^{-4}$	$8.64 \cdot 10^{-4}$	0.87
170	$1.383 \cdot 10^{-3}$	$1.37 \cdot 10^{-3}$	1	$8.476 \cdot 10^{-4}$	$8.402 \cdot 10^{-4}$	0.86
175	$1.399 \cdot 10^{-3}$	$1.385 \cdot 10^{-3}$	1	$8.327 \cdot 10^{-4}$	$8.255 \cdot 10^{-4}$	0.86
180	$1.4 \cdot 10^{-3}$	$1.39 \cdot 10^{-3}$	1	$8.277 \cdot 10^{-4}$	$8.206 \cdot 10^{-4}$	0.86
185	$1.399 \cdot 10^{-3}$	$1.385 \cdot 10^{-3}$	1	$8.327 \cdot 10^{-4}$	$8.255 \cdot 10^{-4}$	0.86
190	$1.383 \cdot 10^{-3}$	$1.37 \cdot 10^{-3}$	1	$8.476 \cdot 10^{-4}$	$8.402 \cdot 10^{-4}$	0.86
195	$1.358 \cdot 10^{-3}$	$1.345 \cdot 10^{-3}$	1	$8.715 \cdot 10^{-4}$	$8.64 \cdot 10^{-4}$	0.87
200	$1.324 \cdot 10^{-3}$	$1.306 \cdot 10^{-3}$	1.3	$9.035 \cdot 10^{-4}$	$8.957 \cdot 10^{-4}$	0.87
205	$1.28 \cdot 10^{-3}$	$1.267 \cdot 10^{-3}$	1	$9.421 \cdot 10^{-4}$	$9.339 \cdot 10^{-4}$	0.87

Table C.6: Comparison of H_{ii} values obtained in 2D by the two methods (30) and (C.1).

loading conditions on crack surface	mode I			mode II			mode III		
calculation method / crack orientation	H_{11}	$H_{11}^{\Omega^*}$	% difference	H_{22}	$H_{22}^{\Omega^*}$	% difference	H_{33}	$H_{33}^{\Omega^*}$	% difference
(100)	$8.42 \cdot 10^{-4}$	$8.47 \cdot 10^{-4}$	0.6	$5.28 \cdot 10^{-4}$	$5.28 \cdot 10^{-4}$	-0.01	$7.94 \cdot 10^{-4}$	$7.97 \cdot 10^{-4}$	0.44
$(-\sqrt{3}10)$	$7.45 \cdot 10^{-4}$	$7.38 \cdot 10^{-4}$	-1	$5.68 \cdot 10^{-4}$	$5.67 \cdot 10^{-4}$	-0.09	$7.38 \cdot 10^{-4}$	$7.34 \cdot 10^{-4}$	-0.59
(-110)	$6.26 \cdot 10^{-4}$	$6.25 \cdot 10^{-4}$	-0.12	$5.95 \cdot 10^{-4}$	$5.85 \cdot 10^{-4}$	-1.7	$6.65 \cdot 10^{-4}$	$6.52 \cdot 10^{-4}$	-1.96

Table C.7: Comparison of H_{ii} values for $\mathbf{half-circular}$ cracks, obtained in 3D by two methods - (30) and (C.1).

loading conditions on crack surface	mode I			mode II			mode III		
calculation method / crack orientation	H_{11}	$H_{11}^{\Omega^*}$	% difference	H_{22}	$H_{22}^{\Omega^*}$	% difference	H_{33}	$H_{33}^{\Omega^*}$	% difference
(-101)	$2.73 \cdot 10^{-4}$	$2.76 \cdot 10^{-4}$	0.95	$1.23 \cdot 10^{-4}$	$1.25 \cdot 10^{-4}$	1.18	$3.15 \cdot 10^{-4}$	$3.16 \cdot 10^{-4}$	0.3
(111)	$2.28 \cdot 10^{-4}$	$2.3 \cdot 10^{-4}$	0.84	$1.76 \cdot 10^{-4}$	$1.77 \cdot 10^{-4}$	0.43	$2.43 \cdot 10^{-4}$	$2.44 \cdot 10^{-4}$	0.31
(212)	$2.59 \cdot 10^{-4}$	$2.62 \cdot 10^{-4}$	0.95	$1.18 \cdot 10^{-4}$	$1.15 \cdot 10^{-4}$	2.1	$2.96 \cdot 10^{-4}$	$2.97 \cdot 10^{-4}$	0.3
$(51(-3))$	$3.82 \cdot 10^{-4}$	$3.85 \cdot 10^{-4}$	0.76	$1.92 \cdot 10^{-4}$	$1.93 \cdot 10^{-4}$	0.2	$3.37 \cdot 10^{-4}$	$3.37 \cdot 10^{-4}$	0.23

Table C.8: Comparison of H_{ii} values for $\mathbf{circular}$ cracks, obtained in 3D by two methods - (30) and (C.1).

loading conditions on crack surface	mode I			mode II			mode III		
calculation method / crack orientation	H_{11}	$H_{11}^{\Omega^*}$	% difference	H_{22}	$H_{22}^{\Omega^*}$	% difference	H_{33}	$H_{33}^{\Omega^*}$	% difference
(100)	$1.04 \cdot 10^{-3}$	$1.03 \cdot 10^{-3}$	-1.2	$5.53 \cdot 10^{-4}$	$5.51 \cdot 10^{-4}$	-0.27	$1.02 \cdot 10^{-3}$	$1.01 \cdot 10^{-3}$	-0.88
$(-\sqrt{3}10)$	$9.13 \cdot 10^{-4}$	$9.01 \cdot 10^{-4}$	-1.44	$6.19 \cdot 10^{-4}$	$6.17 \cdot 10^{-4}$	-0.26	$9.49 \cdot 10^{-4}$	$9.4 \cdot 10^{-4}$	-0.94
(-110)	$7.64 \cdot 10^{-4}$	$7.66 \cdot 10^{-4}$	0.23	$6.57 \cdot 10^{-4}$	$6.68 \cdot 10^{-4}$	1.64	$8.38 \cdot 10^{-4}$	$8.56 \cdot 10^{-4}$	2.08

Table C.9: Comparison of H_{ii} values for $\mathbf{half-elliptical}$ cracks ($a/b = 2$), obtained in 3D by two methods - (30) and (C.1).

The two different methods to compute H_{ii} yield very close results. The relative difference between them can be further reduced by using a larger number of Gauss points. The method based on the potential energy of the spherical (or circular) models is straightforward for pure loading modes and therefore easy to implement for verification purposes of the H_{ii} 's obtained by (30).

References

[1] A. Seweryn. Brittle fracture criterion for structures with sharp notches. *Engrg. Frac. Mech.*, 47(5):673–681, 1994.

[2] F.J. Gomez, M. Elices, F. Berto, and P. Lazzarin. Fracture of V-notched specimens under mixed mode (I+II) loading in brittle materials. *Int. Jour. Fracture*, 159:121–135, 2009.

[3] M.R. Ayatollahi, A.R. Torabi, and P. Azizi. Experimental and theoretical assessment of brittle fracture in engineering components containing a sharp V-notch. *Experimental Mechanics*, 51:919–932, 2011.

[4] A. Sapora, P. Cornetti, and A. Carpinteri. A finite fracture mechanics approach to V-notched elements subjected to mixed-mode loading. *Engrg. Frac. Mech.*, 97:216 – 226, 2013.

[5] A. Sapora, P. Cornetti, and A. Carpinteri. V-notched elements under mode II loading conditions. *Structural Engineering and Mechanics*, 49:499–508, 2014.

[6] Z. Yosibash, E. Priel, and D. Leguillon. A failure criterion for brittle elastic materials under mixed-mode loading. *Int. Jour. Fracture*, 141(1):291–312, 2006.

[7] D Leguillon. Strength or toughness? A criterion for crack onset at a notch. *Eur. Jour. Mech. A - Solids*, 21(1):61–72, 2002.

[8] Z. Yosibash. *Singularities in Elliptic Boundary Value Problems and Elasticity and their Connection with Failure Initiation*. Springer, 2012.

[9] Z. Yosibash, N. Omer, M. Costabel, and M. Dauge. Edge stress intensity functions in polyhedral domains and their extraction by a quasidual function method. *Int. Jour. Fracture*, 136:37 – 73, 2005.